

Residual Circulation in the Stratosphere and Lower Mesosphere as Diagnosed from Microwave Limb

Souder J. et al.

Janusz Pluszkiewicz*

Division of Geological and Planetary Sciences

California Institute of Technology, Pasadena, CA 91125, U.S.A.

David Crisp, Richard Zurek, Lee Elson,

Ivan Vishnien, ancien Proidevaux, and

Earth and Space Sciences Division

Jet Propulsion Laboratory, Pasadena, CA 91109, U.S.A.

Robert Harwood

Department of Meteorology, Edinburgh University, Edinburgh EH9 3JZ, UK.

and Gordon Peckham

Department of Physics, Heriot-Watt University, Edinburgh EH14 4AS, U.K.

submitted to *J. Atmos. Sci.* (U.S. Special Issue)

March 12, 1994

*current address: Center for Meteorology and Physical Oceanography, Massachusetts Institute of Technology, Cambridge, MA 02139 U.S.A.

Abstract

Results for the **residual circulation** in the stratosphere and **lower** mesosphere between September 1991 and February 1994 are reported. This circulation is diagnosed from the measurements of temperature, ozone, and water vapor acquired by the Microwave Limb Sounder (ML S) on-board the Upper Atmosphere Research Satellite, augmented by climatological distributions of methane, nitrous oxide, nitrogen dioxide, surface albedo, and **cloud cover**. An **accurate radiative** transfer code and a streamfunction code that **avoids** the problem of global imbalance in the net diabatic heating rates, are **used** in the calculations. The computed **vertical velocities** undergo a semiannual oscillation (**SAO**) around the tropical stratopause, with the region of downward velocities reaching maximum spatial extent in February and **August**. This behavior is **related** to the semiannual oscillation in temperature and ozone and mimics that seen in past **studies** of the October 1978 - May 1979 period based on data from the Limb Infrared Monitor of the Stratosphere onboard the Nimbus 7 satellite. A possible modulation of the SAO by the quasi-biennial oscillation (QBO) is hinted at. The relation of the computed circulation to existing theoretical models of the SAO is discussed and its possible implications for the distribution of trace constituents are illustrated by the example of the "double-peaked" structure in the water vapor distribution measured by ML S.

1 Introduction

The studies of the diabatic circulation in the middle atmosphere were pioneered by Murgatroyd and Singleton (1961), who used the diabatic heating rates computed by Murgatroyd and Goody (1958). The latter only considered radiative transfer by carbon dioxide and ozone, with the distribution of the latter based on the sparse information available at the time. Even so, the resulting diabatic circulation captured most of the essential features of the “Brewer-Johnson” circulation deduced from early observations of the meridional distribution of ozone and water vapor.

More recent derivations of the zonally symmetric transport in the stratosphere have been based on the transformed Eulerian-mean (TEM), or residual-mean, system of equations, in which the observed temperature field is used to compute time tendency and horizontal heat flux terms, in addition to the infrared cooling needed to determine the net diabatic heating. The advent of nearly global temperature fields retrieved from satellite-borne remote sensors has provided the critical input to these calculations. Of particular note are the diagnostic calculations based on climatologies derived from several satellites (Rosenfield et al. 1987; Callis et al. 1987; Shine 1989; Marks 1989; Choi and Holton 1991) and those based on the observations of the Nimbus 7 and Infrared Monitor of the Stratosphere (ILMS) over the period October 1978 - May 1979 (Solomon et al. 1986; Hitchman and Leovy 1986; Gille et al. 1987; Callis et al. 1987; Pawson and Harwood 1989). The main advantage of the ILMS-based studies was the high vertical resolution of the temperature and constituent data retrieved from ILMS, while the climatological studies had the benefit of investigating the circulation over a full seasonal cycle. The vertical resolution and spatial coverage obtained by ILMS were especially useful in the study of large-scale phenomena like atmospheric tides and the semiannual oscillation (SAO), although only one cycle of the latter was covered during the operational period of ILMS.

The launch of the Upper Atmosphere Research Satellite (UARS) on September 12, 1991 (Reber

et al. 1993) has provided a new data set with the vertical resolution of temperature and constituent measurements comparable to LIMS, but which now extends for several instruments into the third year of nearly continuous observations. The purpose of this paper is to report on the residual circulation computed from ozone, water vapor, and temperature fields retrieved from observations by the UARS Microwave Limb Sounder (MLS) (Waters et al. 1993), which are most complete in their temporal and spatial coverage. Particular emphasis will be given to the SAO because of its prominence in the temperature and ozone fields, and thus in the diagnosed residual circulation.

The formalism used is presented in section 2. The input fields for the diabatic heating calculation are described in section 3, where we also discuss how we deal with one unique aspect of the UARS MLS data, namely the shifting pattern of high-latitude coverage caused by the 57° inclination of the satellite orbit. A description of a sophisticated radiative transfer code is given in section 4. The resulting residual circulation is discussed in section 5. The semiannual oscillation and its implications for stratospheric transport are discussed in section 6. The paper concludes with a summary in section 7.

2 Theoretical Framework

The residual circulation (\bar{v}^* , \bar{w}^*) is of primary importance in two-dimensional stratospheric modeling (see e.g., WMO 1986). It is governed by the TEM equations (Andrews et al. 1987)

$$\frac{\partial \bar{u}}{\partial t} + \left[f + \frac{1}{a \cos \phi} \frac{\partial}{\partial \phi} (\bar{u} \cos \phi) \right] \bar{v}^* + \bar{w}^* \frac{\partial \bar{u}}{\partial z} = \bar{X} + \frac{1}{\rho a \cos \phi} \nabla \mathcal{J} \quad (1)$$

$$\frac{\partial}{\partial t} \left[\frac{1}{a} \frac{\partial \Phi}{\partial \phi} \right] + f \bar{u} + \frac{1}{a} \frac{\partial \Phi}{\partial \phi} = \bar{G} \approx 0 \quad (2)$$

$$\frac{\partial \Phi}{\partial z} + \frac{R\bar{\theta}}{H} e^{-\kappa z/H} = 0 \quad (3)$$

$$-\frac{1}{a \cos \phi} \frac{\partial}{\partial \phi} (\bar{v}^* \cos \phi) + \frac{1}{\rho} \frac{\partial}{\partial z} (\rho \bar{w}^*) = \approx \quad (4)$$

$$\frac{\partial \bar{\theta}}{\partial t} + \frac{\bar{v}^*}{a} \frac{\partial \bar{\theta}}{\partial \phi} + \bar{w}^* \frac{\partial \bar{\theta}}{\partial z} = \bar{Q} - \frac{1}{\rho} \frac{\partial}{\partial z} \left[\rho \left(\bar{v}^* \theta' + \frac{1}{a} \frac{\partial \bar{\theta}}{\partial \theta} \frac{\partial \phi}{\partial z} + \bar{w}^* \theta' \right) \right] \quad (5)$$

The notation is standard. The vector \mathcal{F} appearing on the right-hand side of equation (1) is called the Eliassen-Palm (E-P) flux and its divergence represents the contribution to the zonal momentum from planetary waves, whereas the term \bar{X} denotes the contribution from small-scale waves and other subgrid processes. In equation (2), the term \bar{G} denotes the contribution to the meridional momentum from waves and unresolved processes and is usually neglected. The second term (with the minus sign) on the right-hand side of equation (5) will be referred to as eddy heating and denoted by $\bar{w}^* c^{\kappa z/H}$. The first term \bar{Q} is the net diabatic heating, equal to $(\bar{J}/c_p) e^{\kappa z/H}$, where \bar{J} is the diabatic heating rate per unit mass. In the following, \bar{J}/c_p will be referred to as the “net diabatic heating” and expressed in units of kelvins per day. In the middle atmosphere, this heating is the balance between absorption of solar radiation and emission and absorption of infrared radiation. The availability of an accurate radiative transfer model, in addition to the distributions of temperature and of the radiatively active gases, is essential for computing the net radiative heating rates, since the latter are obtained by subtracting the almost-equal solar heating and thermal cooling rates at each stratospheric level. Thus, small errors in either of these components can produce much larger errors in the net heating rates and in the strength of the derived residual circulation. This is particularly true at levels in the middle and lower stratosphere, where the solar heating and thermal cooling rates often differ by less than 20%. Crisp (1986, 1989, 1990) has developed a variety of accurate methods for finding radiative fluxes and heating rates in scattering and absorbing

planetary atmospheres. We have combined these methods to produce a comprehensive radiative transfer model that can accommodate, with one exception, all radiative processes known to be important in the stratosphere and lower mesosphere, including absorption emission, and multiple scattering by gases, clouds, and aerosols. The application of this model to the present data set is described in section 4

The residual circulation (\bar{v}^* , \bar{w}^*) can be calculated from equations (4) and (5), provided the distributions of temperature and \bar{Q} are known, and the eddy heating term on the right-hand side of equation (5) is neglected or estimated. This term, which represents cross-isentropic heat transport by eddies, is expected to be small in the middle atmosphere (Mitchman and Leovy 1986; Andrews et al. 1987; Gille et al. 1987; C. Marks as quoted by Shine 1989). The findings of our investigation into its magnitude are discussed in section 5. When the eddy heating and temperature tendency terms in equation (5) are neglected, the residual velocity components computed from equations (4) and (5) are referred to as the diabatic circulation (Gille et al. 1987). In this study, the temperature tendency term will be retained and the eddy heating term estimated and then neglected

3 Input Data

3.1 Global Fields from MJS Data

In the present study, the fields of temperature, ozone, and water vapor measured by the MJS instrument will be used in the radiative transfer calculations. These fields are taken from the latest files (Version 3) available at the Central Data Handling Facility at the Goddard Space Flight Center. The methodology of retrieving atmospheric fields from MJS observations is briefly described by Froidevaux et al. (this issue); a more detailed description is being prepared for publication in a special issue describing results of the UARS validation activities. The vertical resolution of MJS

measurements is on the order of 5 km or better. In this investigation, the zonally- and time-averaged fields will be used for the most part. These averages have been obtained as the $\Psi(m = 0, \sigma_n = 0)$ component in the Fourier expansion

$$\psi(\lambda, t) = \sum_{m=0}^M \sum_{n=0}^N \Psi(m, \sigma_n) \exp[i(m\lambda + \sigma_n t)] \quad (6)$$

where the field $\psi(\lambda, t, \phi, z)$ is defined over longitude λ , time t , latitude ϕ , and log- p pressure z , m is the longitudinal wavenumber, and σ_n is the frequency. The Fourier components $\Psi(m, \sigma_n)$ (which are functions of latitude and log-pressure) have been computed from the individual profile data by 11] (tails of an asymptotic mapping technique described by Elson and Froidevaux 1993). This technique, based on the work by Salby (1982) and Lait and Stanford (1988), accounts for the asynchronous nature of the MLS data (i. e., the incomplete spatial and temporal sampling) and the 57° inclination of the UARS orbit.

The inclination of the orbit also restricts the latitudinal coverage of MLS and other UARS measurements. Since the MLS instrument views the atmospheric limb in a direction perpendicular to the orbit track, the latitudinal coverage at any time extends to about 80° in one hemisphere, but to only 34° in the other hemisphere. Approximately once a month, the spacecraft is rotated in a yaw maneuver by 180° in its track, at which point the latitudinal coverage is reversed between the two hemispheres. The period between two consecutive yaw maneuvers is referred to as one UARS month (there are ten UARS months in a year). In order to obtain the global fields necessary for a proper introduction of the boundary conditions on the residual circulation, quasi-biweekly averages corresponding to periods before and after the yaw times are selected for the calculations. These averages are formed as follows. First, the fields of $\Psi(m = 0, \sigma_n = 0)$ (with $\Psi = T, [O_3]$, and $[H_2O]$) are computed for an 7.2-day period (108 orbits) preceeding a yaw maneuver, giving the zonally-averaged distributions of temperature, ozone, and water vapor between 30° in one hemisphere and

90° in the other hemisphere (the values poleward of 80° are obtained by linear extrapolation). Using these distributions, the field of \bar{J}/c_p is computed. Then the corresponding field is computed for an 7.2-day period after the yaw and the results are averaged between 30°S and 30°N, where the south- and north-viewing fields overlap. Poleward of 30° the fields of \bar{J}/c_p prior to or after the yaw are used, as appropriate. The yaw dates considered in this study and their averaging periods are listed in Table 1. The latter are occasionally shorter than 7.2 days due to spacecraft or instrumental problems. The two extreme cases are the periods preceding yaw maneuvers on October 24, 1993, and February 4, 1994, when only two and one day of data are available, respectively. In these two cases, the zonally averaged temperature and ozone fields have been constructed by simple averaging of individual profile (Level 3A1.) data (water vapor data were no longer available at those times, see section 3.4).

3.2 Temperature

Based on validation studies, it is presently believed that MJS temperature retrievals are reliable at pressures greater than 1 hPa. At lower pressures (i.e., higher altitudes), MJS-retrieved temperature gradients may be too steep, leading to a cold bias of up to 10 K at 0.1 hPa. We have explored the possible consequences of this bias by calculating the change in diabatic heating rates when the temperature is increased linearly in log-pressure by 0 to 10 K between and 0.1 hPa and set equal to the value at 0.1 hPa for pressures less than 0.1 hPa (this modification has been applied at all altitudes). For the average of the period February 1-17, 1993, the resulting differences in infrared cooling rates were found to be less than 3% at pressures greater than 0.4 hPa, increasing to 10% at 0.2 hPa, and reaching more than 30% at 0.1 hPa. These differences affected our computed residual circulation at pressures greater than 0.4 hPa only slightly, but the impact of temperature errors on the circulation at lower pressures is in need of further assessment. At pressures greater

than 46 hPa, temperatures provided by the National Meteorological Center (NMC) are utilized, since the O_2 line used for pressure and temperature retrievals becomes saturated.

3.3 Ozone

The MLS instrument measures ozone concentrations at pressures ≤ 100 hPa using emission at 205 GHz. Between 100 and 464 hPa, the ozone abundances are constrained to values obtained from the two-dimensional model of Lawrence Livermore National Laboratory. At lower altitudes, ozone concentrations have been set to the assumed 464-hPa value. This seems to be a reasonable procedure, for three reasons: (1) the main focus of the present study is on the upper stratosphere and lower mesosphere, (2) lower tropospheric ozone abundances are more than one order of magnitude lower than peak stratospheric concentrations, and (3) global measurements of tropospheric ozone are not available. A test calculation for January 1992, in which ozone abundances at pressures greater than 464 hPa were set to zero, produced relative changes of less than 5% in the computed diabatic velocities, except in some regions of near-zero velocities, particularly in the lower stratosphere. We tested the sensitivity of the computed solar heating rates to the accuracy of ozone measurements at pressures less than 1 hPa by replacing the 205 GHz abundances at those altitudes with those measured in the MLS 183 GHz channel. The effect was found to be smaller than 5%, which is less than the estimated accuracy of our solar heating code.

3.4 Water vapor and other constituents

Water vapor concentrations are measured in the 183 GHz channel. For the period between June 2 and July 17, 1992, when the H_2O channel was not operational, climatological values compiled by the UARS Science Team are used. The UARS water vapor climatology below 0.5 hPa is based primarily on the LIMS data (e.g., Russell et al. 1984), assuming some seasonal symmetry to

extend this data base to the northern summer and fall periods not observed by LIMS. The MIS O_2 retrievals are currently considered most reliable in the 46 to 0.2 hPa pressure range; the values at 100 hPa are mostly climatology, as are the values at 46 hPa at high latitudes. After April 25, 1993, when the O_2 channel ceased to operate, the seasonally adjusted fields from the period April 1992 - March 1993 (yaws 7-16 in Table 1) are used.

The MIS fields are augmented by distributions of methane and nitrous oxide from the pre-launch climatology and from the LIMS daytime distribution of NO_2 extended to a full seasonal cycle on the assumption of hemispheric symmetry for the respective season. The tropospheric CO_2 mixing ratio is computed by means of the expressions given by Keeling et al. (1989) and a stratospheric CO_2 concentration of 346 ppmv is assumed. In addition, climatological values of the fractional cloud coverage by high, middle and low clouds are utilized. They have been obtained from the monthly averages distributed by the International Satellite Cloud Climatology Project (ISCCP) (Rossow and Schiffer 1991). Since data for 1992-94 are not available yet, we used interannually averaged data for 1984-86. Cloud-top heights for the three levels were also taken from ISCCP, but we did not use ISCCP-supplied optical thicknesses or cloud types, instead taking all high clouds to be cirrus, all middle-level clouds to be altostratus, and all low clouds to be stratocumulus. Details of the assumed cloud optical properties are given in section 4.

4 Radiative Heating

The input fields are obtained on the standard UARS pressure grid with 31 vertical levels equally spaced in log-pressure between the ground and 0.01 hPa. This yields a vertical resolution of approximately 1/3 scale height (≈ 2.5 km), but since MIS retrievals are performed at every other level, the vertical resolution of our input data is ≈ 5 km. Heating calculations are performed on the same vertical grid at a 5° latitudinal resolution in applications where three-dimensional

input fields are required, the longitudinal resolution is also 5° .

4.1 Solar Heating

The absorption of sunlight by O_3 at UV and visible wavelengths provides the majority of the solar heating at most stratospheric levels, but absorption within near-infrared H_2O , CO_2 , and O_2 bands also produces substantial heating (10 to 30%) in the lower stratosphere. A variety of other gases (N_2O , CH_4 , NO_2) contribute much less solar heating, but are included here for completeness, as is Rayleigh scattering and scattering by tropospheric clouds. Rayleigh scattering indirectly increases solar heating at some levels by increasing the path lengths traveled by solar photons, and decreases it at other levels by reflecting solar radiation back to space before it can be absorbed by the atmosphere or the surface. Tropospheric clouds also produce small increases in the stratospheric heating rates by reflecting sunlight back through the stratosphere for a second pass, again increasing the photon path length and the probability of absorption.

We have combined two different radiative modeling methods to account for the scattering and absorption of sunlight by these processes. At wavelengths outside of the strong near-infrared H_2O , CO_2 , and O_2 absorption bands, where the extinction of sunlight is dominated by Rayleigh scattering and continuum absorption, solar fluxes and heating rates are obtained from a multiple scattering model based on the multilevel δ -Eddington/adding method (Crisp 1986). This approach cannot be used at near-infrared wavelengths within strong gas vibration-rotation bands, because the broadband absorption within these bands does not satisfy the Beer-Bouguer-Lambert Law (Liou 1980; Goody and Yung 1989), as the multiple scattering model requires. We have therefore replaced the δ -Eddington/adding model with a much simpler 2-stream nonscattering model (Crisp 1990) for these spectral regions. The broadband gas absorption at these wavelengths is evaluated by means of a Voigt quasi-random model (Crisp 1990; Santee and Crisp 1993). The absorption

by cloud droplets is also included at these wavelengths, but multiple scattering is neglected. The solar spectrum is divided into 755 spectral intervals, equally spaced in wavenumber between 0.125 and 5.26 microns, in order to resolve the wavelength dependence of the solar flux, of the Rayleigh scattering cross section, and of the absorption coefficients of the gas and cloud absorption features. Spectral intervals occupied by infrared vibration-rotation bands of gases are further subdivided into 2 cm^{-1} intervals to improve the resolution of the band profiles and the accuracy of the product rule (Goody and Yung 1989) which is used to combine absorption by two or more gases that absorb in the same spectral interval. Absorption cross sections for O_3 and O_2 in the visible and UV are taken from DeMore et al. (1990).

Solar fluxes at the top of the atmosphere are taken from Thekaekara (1969). A Lambertian surface is assumed, with the visible albedos taken from ISCCP data. For the near-infrared, we have assumed that the ratio of the surface near-IR albedo to visible albedo depends on surface type and is approximated by the expressions of Briegleb (1992). Latitudinal distributions of surface vegetation have been obtained from the NASA Goddard Institute for Space Studies database (Matthews 1983, 1984) and the ISCCP ice-and-snow fraction is incorporated into the calculation in order to arrive at a probable near-IR albedo for each month and zonal band.

The wavelength-dependent extinction, absorption, and scattering cross sections, and the scattering phase functions for liquid water clouds have been derived by means of a Mie-scattering model which combines a Mie-scattering algorithm (Wiscombe 1980 and 1992, personal communication) with the methods used to integrate over particle size distributions described by Hansen and Travis (1974). Cloud particle size distributions for altostratus (middle) and stratus (low) clouds are taken from Hansen (1971). Refractive indices for liquid water are taken from Hale and Querry (1973). For cirrus clouds, we use the wavelength-dependent optical properties for columnar ice columns (Freeman and Liou 1979). The nominal visible optical depths for each cloud type are from Stephens

(1978).

Despite enhanced aerosol concentrations in the stratosphere during the early months of the UARS mission caused by the eruption of Mt. Pinatubo, the presence of aerosols is ignored. This neglect has been prompted by the desire to obtain a data base heating rates for comparison with past work and for future reference and by the difficulty in obtaining global estimates of aerosol properties and abundances. As aerosol opacities and other optical properties become available from measurements by ground-based, aircraft, satellite, and other UARS instruments, it will be possible to include aerosol effects in the calculations, with one caveat: our code is not designed to handle simultaneous multiple scattering and nongray absorption, which is important in the presence of the Pinatubo sulfate aerosols.

4.2 Infrared Cooling

Absorption and emission within the strong CO_2 15- μm band and the O_3 9.6- μm band dominate the thermal flux divergences and cooling rates at most stratospheric levels. A variety of other gases included in the model also absorb and emit thermal radiation, but their contributions to the stratospheric cooling rates are much smaller. High-altitude tropospheric clouds affect the thermal cooling rates within the lower stratosphere by modulating the upward flux of thermal radiation from the warm surface and lower troposphere, but the relatively low single scattering albedo of water droplets and ice crystals at these wavelengths reduces the importance of multiple scattering. This substantially decreases the complexity and computational expense of the thermal radiative modeling methods.

To account for the thermal radiative processes listed above, the radiative transfer model includes absorption by gases (H_2O , CO_2 , O_3 , N_2O , CH_4 , O_2 , NO_2) and clouds, but neglects multiple scattering. A Voigt quasi-random model (Crisp 1989, 1990) is used to find gas transmission functions

within spectral intervals occupied by vibration-rotation bands. The method described by Roberts et al. (1976) is used for water vapor continuum absorption. Clouds and aerosols are treated as continuum absorbers within each thermal infrared spectral interval and their transmission is obtained from Beer's law. The solution to the thermal equation of transfer is similar to that described by Crisp (1989, equations (5)-(9)), except that we have modified the surface boundary condition to include a non-unit emissivity, and a temperature gradient between the surface and the first atmospheric level above the surface (Crisp 1990, equation (14)). In the calculations reported here, the two-stream, diffusivity-factor approach for approximating the upward and downward thermal fluxes is used, but our code can also apply the more rigorous multistream method, in which thermal radiances are obtained along 8 streams and gaussian quadrature is used to integrate the radiances over zenith angle, i.e., the model computes thermal radiances along 4 upward streams and 4 downward streams, and the thermal flux integrals for the upper and lower hemisphere are evaluated using a 4-point gaussian quadrature.

The thermal spectrum between 5.26 and 250 microns is divided into 95 spectral intervals in order to resolve gas absorption bands and the wavelength dependence of the Planck function. As in the solar flux calculation, spectral intervals occupied by gas vibration-rotation bands are further subdivided into 2 cm^{-1} intervals to better resolve band contours and to improve the accuracy of the product rule. Gas absorption line parameters at infrared wavelengths are taken from the 1992 edition of the HITRAN database (Rothman 1992). Thermal infrared surface albedos are taken from Warren (1982) for snow, assumed to be zero for dry land, and calculated explicitly for ocean, including the effect of increased sea-surface roughness as one goes from the tropics to high latitudes.

The high accuracy of our thermal infrared code under clear-sky conditions is documented in Fig. 1. This figure also shows that most of our conclusions would in fact be valid if only clear-sky situations with three radiative gases (H_2O , CO_2 , and O_3 , and a single surface albedo of 0.3 were

considered. That is, the other gases as well as tropospheric clouds and the distribution of surface albedo can be regarded as “embellishments” to the zeroth order effects provided by the three main gases. It is the extensive temporal and spatial coverage and the high vertical resolution of MLS temperature, ozone, and water vapor measurements which constitute the most valuable asset of the present study.

5 Residual Circulation

The net diabatic heating rates \bar{Q} are obtained as the sum of solar heating and infrared cooling rates, calculated in the manner described in section 4. Given \bar{Q} , the vertical and meridional components of the residual circulation (\bar{v}^* , \bar{w}^*) are computed from equations (4) and (5). The $\partial\bar{T}/\partial t$ term has been computed by differentiating equation (6) with respect to time, forming the daily global maps of $\partial T/\partial t$, and averaging both along latitude circles and over a 6-day period (i.e., of the 8 daily synoptic maps formed from the 7.2-day averages, the first and last are excluded). Since we are not interested in 1-2 day variability in the construction of global fields, spectral components with $\sigma_n \geq 6.09$ day⁻¹ (i.e., periods ≤ 1.032 days) have been excluded in forming the maps. For the periods October 22-23, 1993 and January 25, 1994, which are too short to permit computation of reliable Fourier coefficients, the distribution of $\partial T/\partial t$ has been set to zero. The distribution of $\partial\bar{T}/\partial t$ for the period February 1-17, 1993, is shown in Figure 2a. By and large, $\partial\bar{T}/\partial t$ can also be considered to be an “embellishment” in this study. Without global measurements of meridional and vertical winds, the eddy heating term \bar{E} cannot be calculated directly. We have employed two methods to estimate the contribution to \bar{E} from planetary scale eddies. In the first method, this term has been computed from the three-dimensional wind fields provided by the UK Meteorological Office and produced through a data assimilation procedure applied to conventional meteorological data, including data from the NOAA Stratospheric Sounding Unit (Swinbank and O’Neill 1994).

These fields are available for the second UARS year beginning 011 September 13, 1992. In the Second method, $\bar{E}e^{\kappa z/H}$ has been approximated by the formula

$$-\frac{1}{\rho} \frac{\partial}{\partial z} \left[\rho \left(\bar{v}' \bar{\theta}' \frac{1}{a} \frac{\partial \bar{\theta}}{\partial \phi} + \bar{w}' \bar{\theta}' \right) \right] = -\frac{1}{\rho} \frac{\partial}{\partial z} \left[\frac{\rho}{\partial \bar{\theta} / \partial z} \left(\bar{Q}' \bar{\theta}' + \frac{1}{2} \frac{\partial \bar{\theta}'^2}{\partial t} \right) \right] \quad (7)$$

which can be obtained from the linearized thermodynamic equation, provided the terms in the equation representing advection by zonally averaged meridional and vertical winds are negligible. Since the evaluation of the right-hand side of the above equation requires the knowledge of the three-dimensional field of net diabatic heating, the availability of a radiative transfer code faster than ours is essential for this task. We have chosen for this purpose the code developed by Shine (1987) and the three-dimensional fields of ozone, temperature, and temperature tendency obtained in a manner similar to that described above for $\partial \bar{T} / \partial t$ (i.e., with the first and last days excluded in forming the time average over a given period and excluding spectral components with $\sigma_n \geq 6.09$ day⁻¹). The distributions of \bar{E} obtained by the two methods for the period of February 1-17, 1993, are shown in Figure 2b and 2c, respectively, together with the distribution of net heating \bar{J}/c_p (Figure 2d). We have chosen this period for illustrative purposes, since the atmosphere was highly disturbed at that time and the corresponding values of E are particularly large. As can be seen, E is not negligible in comparison to \bar{J}/c_p , especially at high latitudes around 10 hPa. However, the retention of this term in equation (5) changes the distributions of (\bar{v}^*, \bar{w}^*) only slightly, outside of the winter high latitudes in the lower stratosphere. Since the main focus of this paper is on the equatorial upper stratosphere and lower mesosphere, we have neglected this term in the subsequent calculations. It is interesting to note that the two methods of calculating E give qualitatively similar results in the upper stratosphere. The disagreement at lower altitudes may reflect the inadequacy of approximation (7) under disturbed conditions, the uncertainties in assimilated fields (e.g., w'), or differences in the computed diabatic heatings due to different algorithms and inputs.

Equations (4) and (5) are solved by means of a numerical approach developed by I{-I J. Shia and M. Santee, in which a streamfunction χ^* is introduced

$$\bar{v}^* = -\frac{1}{\cos\phi} e^{z/H} \frac{\partial}{\partial z} \left(e^{-z/H} \chi^* \right) \quad , \quad \bar{w}^* = -\frac{1}{a \cos\phi} \frac{\partial \chi^*}{\partial \phi} \quad (8)$$

and the thermodynamic equation is differentiated with respect to latitude. The resulting streamfunction equation (equation (20) in Santee 1993) is solved by a matrix inversion technique, with the boundary conditions $\chi^* = 0$ at the poles introduced naturally. Thus the scheme avoids numerical instabilities associated with integrating the undifferentiated streamfunction equation from pole to pole. In addition, a major advantage of this approach is that it avoids the problem of any global imbalance between heating and cooling rates, a problem which has been shown to have serious consequences for the resulting diabatic circulation (Shine 1989) (however, the present approach does not alleviate the problem of any errors in the meridional gradients of the net heating rates). The calculations of (\bar{v}^*, \bar{w}^*) are performed on a grid spaced 5° in latitude and 2 km in log-pressure altitude. No-flow boundary conditions are applied at $z = 74$ km (0.02 hPa) and at the poles. At $z = 16$ km (100 hPa), the condition expressed by equation (19) in Santee (1993) is applied. essentially, this condition amounts to specifying \bar{w}^* at the lower boundary (via the thermodynamic equation), but unlike Garcia and Solomon (1983), who imposed \bar{w}^* externally, our matrix inversion technique enables us to determine \bar{w}^* at 100 hPa self-consistently. While \bar{w}^* so obtained cannot account for the total mass flux at 100 hPa, especially in the tropics, it may still be an interesting quantity to compare with the values from Garcia and Solomon (1983), Holton (IWO), and Rosenlof and Holton (1993) and we plot \bar{w}^* at 100 hPa, averaged for each of the four seasons, as a function of latitude in Figure 3. Our method of computing \bar{w}^* , based on the radiation budget, is expected to be more reliable than past estimates, given the high accuracy of our radiative transfer model. However, as discussed earlier, uncertainties may still be large at 100 hPa, given uncertainties and the ill-

simultaneity of our input fields and the neglect of aerosols in the early UARS period. Our approach complements the method of Holton and Rosenlof and Holton, who used the momentum equation and the “downward control principle” to calculate \bar{w}^* at 100 hPa. The values of the extratropical downward mass flux at 100 hPa, averaged for the four seasons, are listed in Table 2, together with the values from Rosenlof and Holton. An estimate of the accuracy of our values is provided by the annual global average of the mass flux at 100 hPa, which is $\approx 4 \times 10^8 \text{ kg s}^{-1}$. Our wintertime values are similar to Rosenlof and Holton’s in the NH, but are roughly a factor of 2 larger in the SH. Our summertime values are essentially zero, in contrast to the results of Rosenlof and Holton. In SON we obtain much more contrast between the hemispheres than Rosenlof and Holton do, and in MAM we obtain more downward flux in SH than in NH, contrary to their results.

In the following, all distributions will only be shown between 100 and 0.2 hPa, with the upper boundary being determined by the quality of MJS data. The extension of the calculations to pressures less than 0.2 hPa (where our temperatures assume climatological values corresponding to the a priori guess in the MJS inversion algorithm) is necessary in order to avoid spurious results at the upper boundary. We have verified that the circulation at pressures greater than 0.2 hPa changes very little when $\chi^* = 0$ is assumed anywhere above $z \approx 68 \text{ km}$. The same holds true for pressures less than $\approx 80 \text{ hPa}$ when a no-flow boundary condition is applied at 100 hPa and this provides some perspective on the effect of “embellishments” discussed earlier.

In addition to the residual circulation, the zonally averaged zonal velocity at latitudes greater than 5° is computed using the gradient wind relationship, i.e., equation (2) with $G = 0$, and the geopotential fields computed from MJS temperatures and the 100-hPa reference level obtained from the National Meteorological Center. Following Marks (1989), we chose the root with the smaller absolute value of \bar{u} . The zonal wind at the equator is obtained by interpolation, as was done by Hinchman and Levy (1986). Given the three TEM velocity components, it is possible

to calculate the right-hand side of equation (1) and thus the forcing of the circulation (Hartmann 1976; Shine 1989). This forcing is the sum of contributions from planetary and small scale waves. It is thought that the former dominate in the stratosphere, but their contribution $(1/\rho a \cos \phi) \nabla \mathcal{F}$ cannot be separately determined in a zonally-averaged approach.

Figures 4-8 show the computed distributions of the zonally averaged gradient wind, the mass-weighted streamfunction $X^* \equiv 2\pi a \rho_s e^{-z/H} \chi^*$, the meridional and vertical components of the residual circulation), and the zonal momentum residual, respectively. The time derivative of gradient wind required for the calculation of the momentum residual is computed by differentiating the gradient wind equation with respect to time and using the fields of $\partial \bar{T} / \partial t$ computed from equation (6), together with the time derivative of the geopotential height at 100 hPa computed by finite differencing. The gross features in Figures 4-8 are quite similar in the three UARS years. The particular features for each of the five fields will be discussed in turn.

5.1 \bar{u}

The northern hemisphere westerlies are weak in January 1992 and January 1994, a manifestation of minor stratospheric warmings. The final warming in the southern hemisphere is well underway by the end of October. In January, a strong easterly jet with velocities in excess of 100 m/s is present at southern subtropical latitudes in the lower mesosphere and upper stratosphere. In February, a residual core of easterlies resides around 2 hPa at 10°S. Similarly strong easterlies were computed at the same location by Hitchman (1985) for January 1979, based on LIMS temperatures. In his study, the residual core of easterlies in February 1979 resides around 7 hPa at 10°S. Our study shows that an easterly jet also forms in the lower mesosphere and upper stratosphere at northern subtropical latitudes in July, but the maximum velocities are somewhat reduced compared with January.

5.2 X^* and \bar{v}^*

The Brewer-Dobson circulation (upwelling in low- to mid-latitudes, downwelling at high latitudes) can clearly be seen in the distribution of X^* . In March, the southern branch of the Brewer-Dobson circulation intrudes into the northern hemisphere around the stratopause. In the wintertime hemisphere, \bar{v}^* is large at subtropical and mid-latitudes around the stratopause, forming a jet-like feature with two branches in the upper stratosphere and lower mesosphere. The peak values of \bar{v}^* in the jet in January are almost a factor of 2 higher than those diagnosed for July. Our peak values in the lower mesospheric branch of the jet in January 1992 (up to 5 m s^{-1}) are similar to those of Hitchman and Leovy (1986), who diagnosed a similar jet-like feature in the lower mesosphere from LIMS data (see their Figure 16), but did not diagnose the upper stratospheric branch of the jet. A hint of a lower mesospheric jet is also present in the other LIMS-based studies by Solomon et al. (1986) and Gille et al. (1987), but their peak values are roughly a factor of 2 lower than ours. A wintertime lower mesospheric jet also was present in the climatological studies by Rosenfield et al. (1987) and Callis et al. (1987). As pointed out by Callis et al., whether or not strong poleward flows are obtained depends, especially in the polar night, on the use of a detailed infrared cooling code and they would not be seen if a Newtonian code were used. One of us (JF) has found out during his ongoing research at MIT that a wintertime jet around the stratopause is present in the distribution of \bar{v}^* calculated using winds from the GFDL "SKYHI" general circulation model. This model jet is co-located with a region of weak mixing diagnosed by analyzing Lagrangian trajectories of air parcels, which suggests that the presence of a region of strong \bar{v}^* may have implications for the dispersal of chemical constituents.

In January-February and in July-August, our distribution of \bar{v}^* shows a structure with two maxima close to the upper boundary of the domain (again, the values for January are a factor of 2 higher than those for July). The maxima are located at $50\text{-}60^\circ$ and $20\text{-}30^\circ$ in the winter- and

summertime hemisphere, respectively. A similar "double-peaked" structure was diagnosed for the winter of 1979 in the LIMS-based studies, with the peak values of Hitchman and Leovy similar to ours (in excess of 7 m s^{-1}) and those of Solomon et al. and Gille et al. a factor of 2 lower. However, we wish to emphasize that the reality of our strong meridional flows in the mesosphere is in need of further assessment in view of the uncertain quality of MLST temperature data at pressures lower than 0.4-0.2 hPa.

5.3 \bar{w}^*

The downwelling branch of the Brewer-Dobson circulation extends to greater heights in the winter hemisphere and is probably connected to a mesospheric cross-equatorial cell (Leovy 1964). Strong (in excess of 16 mm s^{-1}) downward velocities at high latitudes in the wintertime lower mesosphere are a feature our study shares with that of Solomon et al. (1986). As expected, wintertime downward velocities in the stratosphere are greater in the north, since the greater wave activity during northern winter leads to larger departures from radiative equilibrium and thus to larger diabatic cooling rates. On the other hand, the field of \bar{w}^* is very symmetric between the north and the south during summer and fall. During spring, downward velocities at high latitudes are larger in the southern hemisphere.

In the tropics, a region of downwelling exists in the upper stratosphere and lower mesosphere during northern and southern winters. From December through February, this region expands downward from a level in the mesosphere. This behavior mimics that obtained by Hitchman and Leovy (1986), who computed the residual circulation using LIMS data. A region of downwelling around the tropical stratopause was also computed by Solomon et al. (1986) and Gille et al. (1987), again based on LIMS data. On the other hand, it was not obtained in the studies based on climatological data, since the coarse vertical resolution of the climatological temperature fields, as

well as the monthly averaging used to obtain those fields, tend to reduce the amplitude of vertical temperature contrasts (Hitchman 1985). As discussed by Hitchman and Leovy, the presence of a region of downwelling around the tropical stratopause is related to the high-temperature phase of the semiannual oscillation (SAO). The season of maximum temperatures at the tropical stratopause corresponds to a time of maximum diabatic cooling (since at those altitudes cooling is dominated by the cooling-to-space mechanism), as well as to a time of minimum solar heating (since temperature and ozone are anti-correlated). In a *diagnostic* calculation, these two effects lead to a maximum in the net diabatic cooling, and thus a maximum in the downward vertical velocities (but see section 6 for a discussion of cause and effect in this case).

5.4 Zonal momentum residual

As expected, the sign of the residual in the mesosphere is mostly opposite to that of the zonal wind, which is consistent with small-scale drag. The magnitude of the drag at mid- and high latitudes in the wintertime lower mesosphere (in excess of $70 \text{ m s}^{-1} \text{ day}^{-1}$ in January) is significantly greater than in previous studies (Shine 1989; Choi and Holton 1991), mainly as a result of our higher values of \bar{v}^* (since, at those latitudes, the major contribution to the residual is from the $-f\bar{v}^*$ term). The drag is smaller during southern winter. In the northern hemisphere, regions of enhanced drag exist around 1.5, 4 and 10 hPa at mid- and high latitudes during fall and winter. These regions are likely to be the locations where planetary waves break. Similar regions exist in the southern hemisphere, but in July-August they tend to be weaker than their counterparts in January-February.

G SAO and Stratospheric Transport

The SAO signal in \bar{w}^* discussed in section 5.3 has been diagnosed from the observed distribution of temperature and ozone. This diagnostic result does not imply, however, a cause-and-effect relationship between T and \bar{w}^* . Rather, the distribution of T is a result of dynamical effects (represented by \bar{w}^*) and radiative effects resulting from the annual cycle in the solar heating rates (Andrews et al. 1987). Following Geller et al. (1992), the regions of the middle atmosphere where these two effects dominate can be delineated by computing the correlation coefficient r between T and \bar{w}^* . The distribution of r for the first 25 UARS months is shown in Fig. 9. In the stratosphere, this distribution bears a striking resemblance to the distribution computed by Geller et al. from climatological data for 1978-86 (see their Fig. 3). In particular, T and \bar{w}^* are strongly anticorrelated in the tropics and positively correlated at higher latitudes. The tropical anticorrelation implies dynamical control of temperature: rising residual motions give rise to cold temperatures and descending motions give rise to warm temperatures. In the extratropics, on the other hand, the temperatures are primarily under radiative control: warm in summer and cold in winter, with the season of cold temperatures coinciding with the season of strong downward \bar{w}^* (this downward motion causes the temperatures to be higher than they would be in the absence of dynamical effects). Our distribution of r differs significantly from that of Geller et al. above the stratopause: in the tropics the anticorrelation between T and \bar{w}^* extends into the mesosphere at a high confidence level and, in addition, there are indications of anticorrelation at all latitudes at pressures less than 0.3 hPa.

The dynamical processes controlling tropical temperatures are still somewhat uncertain. Geller et al. argued for an upward effect of the Hadley circulation and its variations. Yulaeva et al. (1994) presented arguments that the annual component of the tropical temperature variations in the lower stratosphere is caused by extratropical wave processes. On the other hand, in the tropical upper

stratosphere and lower mesosphere the largest signal in the temperature variations has a semiannual periodicity and the high degree of anticorrelation seen for that region in Fig. 9 is likely to be a manifestation of the SAO. With this in mind, we now turn to a discussion of the SAO in the hfl,S-derived fields.

(3.1 Equatorial SAO

In order to better illustrate the equatorial semiannual oscillation (SAO), in Figure 10 we show the time-height sections of temperature, ozone, water vapor, gradient wind, the net diabatic heating, the meridional and vertical components of the residual circulation, the meridional advection of zonal momentum, and of the zonal momentum residual, averaged in the 5°S-50N latitude band. The fields of T , O_3 , and \bar{u} , besides exhibiting a clear SAO signal in the upper stratosphere and lower mesosphere, show a possible quasi-biennial oscillation (QBO) in the middle and lower stratosphere. A possible QBO signal is also present in the time series of \bar{w}^* , in addition to a strong SAO signal. The anti-phase relationship in the SAO signals for ozone and water vapor are consistent with the opposite vertical gradients for the two species. The annual cycle dominates the time evolution of \bar{v}^* . The extreme values of \bar{w}^* are -6.5 and 3.7111111 s^{-1} and are thus even larger than the values obtained by Choi and Holton (1991) in their scheme modified to enhance the equatorial vertical velocities (see their Figure 12). Our equatorial vertical velocities peak in January and August, respectively, with their magnitudes being smaller in August. This time asymmetry between the two SAO cycles is consistent with forcing by planetary waves, whose activity is greater during northern winter. The time-mean momentum residual is westerly in the lower mesosphere, which is consistent with steady background forcing by eastward-propagating waves, such as Kelvin waves (Andrews et al. 1987). The residual has a semiannual component in the lower mesosphere and upper stratosphere (in particular between 0.2 and 0.3 hPa and between 1 and 2 hPa), with maximum westerly residual

during northern and southern winters. As in the Hitchman and Leovy (1986) study, the largest contribution to the momentum residual is from the meridional advection term, but other terms are also important (in particular, the negative residual in early 1993 is due to the $\partial \bar{u} / \partial t$ term).

Several other features seen in Figure 10 are worth mentioning. Time mean easterlies prevail in the stratosphere, reaching a maximum around 2 hPa, but in the mesosphere the mean wind is westerly. Our vertical profile (not shown) of the time mean of \bar{u} roughly agrees with the profile presented by Reed (1966) in his pioneering study of the SAO, except that our mesospheric westerlies are even stronger than his, exceeding 20 m s^{-1} at pressures less than 0.3 hPa. This equatorial superrotation requires an influx of westerly momentum by waves. Vertically propagating Kelvin waves are a likely candidate for producing mesospheric time mean and SAO westerlies, although Hitchman (1985) concluded that the Kelvin waves observed by LIMS contribute ~ 10 more than 500% of the required westerly momentum, thus implying a possible contribution from vertically propagating small scale gravity waves. A theoretical study of the forcing of the westerly phase of the SAO by Kelvin waves was conducted by Dunkerton (1979). He noted that for a certain range of phase speeds and momentum fluxes at the tropopause, the SAO should be modulated by the QBO, with the SAO westerlies reaching lower altitudes and linking up with the QBO westerlies during the easterly phase of the QBO (the latter being usually defined as the prevailing wind at 30 hPa). Such is the situation in our study (see Figure 10d). This qualitative agreement is certainly encouraging, despite the fact that our study is restricted to just one QBO cycle, and it should provide motivation for further studies of the westerly phase of the SAO using MLS-observed waves. As for the easterly phase, we note that the onset of SAO easterlies tends to occur simultaneously over a deep layer, which seems to be inconsistent with forcing by vertically propagating waves. Instead, meridional advection of easterly momentum and/or absorption of horizontally propagating stationary Rossby waves near the zero-wind line are commonly invoked

to explain the easterly phase. However, in several modeling studies the advection mechanism, while important right at the equator, proved to be incapable of producing easterlies as far as 20 degrees from the equator (Meyer 1970; Holton and Wehrbein 1980; Takahashi 1984), thus implying a greater role for the critical line absorption (Hopkins 1975). We note that our wintertime easterlies do in fact reach 20°. If critical-line absorption is important, then one would expect large values of $(1/\rho a \cos \phi) \nabla \mathcal{F}$, and thus of the momentum residual, in the vicinity of the zero-wind line. A close inspection of Fig. 8 does indeed reveal the presence of regions of enhanced momentum residual around the stratopause near 20°N and 20°S in January and July, respectively.

6.2 implications for stratospheric transport

The implications of the tropical SAO for the distribution of chemical tracers have been studied by Solomon et al. (1986), Gray and Pyle (1986), Gille et al. (1987), and Choi and Holton (1991). In particular, those investigators noted the role played by the region of downwelling in producing the “double-peaked” structure in the distributions of water vapor, nitrous oxide, and methane. The distribution of water vapor measured by MLS is shown in Figure 11. It shows a “double-peaked” structure in low latitudes in the March–May period of 1992 and 1993 and in October 1992. The fact that the double peak is more pronounced around the vernal equinox, with H₂O mixing ratios exceeding 7 ppmv at 1 hPa at the equator in March and the double peak missing entirely in the fall of 1991, seems to be consistent with the vertical velocities at the equatorial stratopause being larger during the northern winter phase of the SAO. The morphology of the region of negative \bar{w}^* at low latitudes is also different during the two SAO phases: during southern winter this region is smaller and is overlaid by a region of upward velocities. In the present study, the downward velocities at the equatorial stratopause do exceed 1 mm s⁻¹ in March (in March 1993 they even exceed 2 mm s⁻¹), as required by Choi and Holton in order to produce the equinoctial double peak

in the distribution of nitrous oxide. Our vertical velocities are slightly negative in the equatorial upper stratosphere as late as April, whereas Choi and Holton were unable to sustain large negative \bar{w}^* in their study, mainly because the SAO signal in the climatological fields of temperature they used was too small. One notable difference between the double peak in the water vapor distribution observed by LIMS and MLS is the vertical extent of this feature, which extends down to almost 10 hPa in the LIMS field, but only to about 2 hPa in the MLS distribution. The deep vertical extent of the LIMS double peak proved difficult to simulate with the residual circulation diagnosed from LIMS (Solomon et al. 1986, Gille et al. 1987), since in the latter the equatorial downwelling only extended down to about 1-2 hPa. On the other hand, if the smaller vertical extent of the MLS water vapor double peak is real, then it should be easier to simulate with our residual circulation, whose downward branch at the equator also extends down to about 2 hPa. The full linkage between the SAO and the “double-peaked” structure can only be established by means of a chemical tracer model and we intend to run such a model, with our residual circulation] used as input, in the near future. We conclude this section by noting a link between SAO and ozone: stratospheric models based on climatologically diagnosed residual circulation fail to reproduce the observed methane distribution (Yang et al. 1991), another species with a “double-peaked” structure, and this may contribute, via its effect on the resulting ClO distribution, to the long-standing “ozone-deficit” problem (Fluszkiewicz and Allen 1993).

7 Summary

With the advent of the Upper Atmosphere Research Satellite ((JARS), it has become possible to study the residual circulation)) in the middle atmosphere at high vertical resolution over several seasonal cycles. In this paper, this circulation has been diagnosed from measurements acquired by the Microwave Limb Sounder onboard UARS. The vertical component of this circulation undergoes

a semiannual oscillation (SAO) in the tropical upper stratosphere and lower mesosphere, which is related to the SAO in temperature and ozone. Our results indicate a possible modulation of the SAO by the quasi-biennial oscillation in the middle and lower stratosphere, which is consistent with existing theoretical models of the forcing of the westerly phase of the SAO by Kelvin waves. The latitudinal extent of wintertime easterlies, as well as the analysis of the zonal momentum residual, suggest a relatively minor role of the meridional advection of easterly momentum in forcing the easterly phase of the SAO. The computed circulation should lead to improvements in the two-dimensional modeling of constituents exhibiting a “double-peaked” distribution in low- and mid-latitudes, in particular water vapor and methane. Since the latter controls the upper stratospheric ClO abundances, these improvements should ultimately lead to better models of ozone.

Acknowledgments

M. F. Gerstell is thanked for her assiduity in assembling the cloud and albedo climatology. I. Fung provided us with information on the NASA GISS database and S. Massie with the information about the CO₂ concentrations. M. Delitsky assisted in the creation of the Fourier coefficient files from which temperature and constituent fields were constructed. M. Santee has provided us with the streamfunction code and G. Manney with the 100-hPa geopotential heights and the UKMO meteorological fields. K. Shine is thanked for the permission to use his radiative transfer code. Comments by A. Plumb are appreciated, in particular his suggestion about the lower boundary condition for the streamfunction equation. R. Atkinson helped with the graphics at MIT. J. Luu is thanked for data management and help with the graphics at JPL. This research was carried out as part of UARS Investigations at JPL/Caltech under contract with NASA and at Edinburgh and Heriot-Watt Universities sponsored by SERC.

References

- Andrews, D. G., J. R. Holton, and C. B. Leovy, 1987: *Middle Atmosphere Dynamics*. Academic Press.
- Briegleb, B. P., 1992: Delta-Eddington approximation to solar radiation in the NCAR Community Climate Model. *J. Geophys. Res.*, 97, 7603-7612.
- Callis, L. B., R. F. Bougher, and J. D. Lambeth, 1987: The stratosphere: Climatologies of the radiative heating and cooling rates and the diabatically diagnosed net circulation fields. *J. Geophys. Res.*, 92, 5555-5607.
- Choi, W. K. and J. R. Holton, 1991: Transport of N_2O in the stratosphere related to the equatorial semiannual oscillation. *J. Geophys. Res.*, 96, 22,543-22,557.
- Crisp, D., 1986: Radiative forcing of the Venus mesosphere. I. Solar fluxes and heating rates. *Icarus*, 67, 484-514.
- Crisp, D., 1989: Radiative forcing of the Venus atmosphere. II. Thermal fluxes, cooling rates, and radiative equilibrium temperatures. *Icarus*, 77, 391-413.
- Crisp, D., 1990: Infrared radiative transfer in the dust-free martian atmosphere. *J. Geophys. Res.*, 95, 14,577-14,588.
- DeMore, W. B., S. P. Sander, D. M. Golden, M. J. Molina, R. F. Hampson, M. J. Kurylo, C. J. Howard, and A. R. Ravishankara, 1990: Chemical Kinetics and Photochemical Data for Use in Stratospheric Modeling. *JPL Publ.*, JPL 90-1.
- Dunkerton, J., 1979: On the role of the Kelvin wave in the westerly phase of the semiannual zonal wind oscillation. *J. Atmos. Sci.*, 36, 372-41.

- Elson, I. S. and L. Froidevaux, 1993: Use of Fourier transforms for asynoptic mapping: Applications to the Upper Atmosphere Research Satellite Microwave Limb Sounder. *J. Geophys. Res.*, 98, 23,039-23,049.
- Eluszkiewicz, J. and M. Allen, 1993: A global analysis of the ozone deficit in the upper stratosphere and lower mesosphere. *J. Geophys. Res.*, 98, 1069-1082.
- Freeman, K. J. and K.-N. Lieu, 1979: Climatic effects of cirrus clouds. *Adv. Geophys.*, 21, 231-287.
- Froidevaux, L., J. W. Waters, W. G. Read, L. S. Elson, D. A. Flower, and R. F. Jarnot, 1994: Global ozone observations from UARS MLS: An overview of zonal mean results. *J. Atmos. Sci.* (this issue)
- Garcia, R. R. and S. Solomon, 1983: A numerical model of the zonally averaged dynamical and chemical structure of the middle atmosphere. *J. Geophys. Res.*, 88, 1379-1400.
- Geller, M. A., E. R. Nash, M.-F. Wu, and J. A. Rosenfield, 1992: Residual circulations calculated from satellite data: Their relations to observed temperature and ozone distributions. *J. Atmos. Sci.*, 49, 1127-1137.
- Gille, J. C., L. V. Lyjak, and A. K. Smith, 1987: The global residual mean circulation in the middle atmosphere for the northern winter period. *J. Atmos. Sci.*, 44, 1437-1452.
- Goody, R. M. and Y. L. Yung, 1989: *Atmospheric Radiation: Theoretical Basis*. Oxford University Press.
- Gray, L. J. and J. A. Pyle, 1986: The semi-annual oscillation and equatorial tracer distributions. *Quart. J. Roy. Meteorol. Soc.*, 112, 387-407.

- Hale, G. M. and M. R. Querry, 1973: Optical constants of water in the 200-nm to 200- μ m wavelength region. *Appl. Opt.*, 12, 555-563.
- Hansen, J. E., 1971: Multiple scattering of polarized light in planetary atmospheres. Part II. Sunlight reflected by terrestrial water clouds. *J. Atmos. Sci.*, 28, 1400-1426.
- Hansen, J. E. and L. D. Travis, 1974: Light scattering in planetary atmospheres. *J. Space Sci. Res.*, 16, 527-610.
- Hartmann, D. L., 1976: The dynamical climatology of the stratosphere in the southern hemisphere during late winter 1973. *J. Atmos. Sci.*, 33, 1789-1802.
- Hitchman, M. H., 1985: *An observational study of wave-mean flow interaction in the equatorial middle atmosphere*. Ph.D. thesis, University of Washington, Seattle.
- Hitchman, M. H. and C. B. Leovy, 1986: Evolution of the zonal mean state in the equatorial middle atmosphere during October 1978 - May 1979. *J. Atmos. Sci.*, 43, 3159-3176.
- Holton, J. R., 1990: On the global exchange of mass between the stratosphere and troposphere. *J. Atmos. Sci.*, 47, 392-395.
- Holton, J. R. and W. M. Wehrbein, 1980: A numerical model of the zonal mean circulation of the middle atmosphere. *Pure Appl. Geoph.*, 118, 284-306.
- Hopkins, R. H., 1975: Evidence of polar-tropical coupling in upper stratospheric zonal wind anomalies. *J. Atmos. Sci.*, 32, 712-719.
- Keeling, C. D., R. B. Bacastow, A. F. Carter, S. C. Piper, T. D. Whorf, M. Heimann, W. G. Mook, and H. Roeloffzen, 1989: A three-dimensional model of atmospheric CO₂ transport based on observed winds: 1. Analysis of observational data. In *Aspects of Climate Variability in the*

- Pacific and Western Americas*, edited by D. H. Petersen, Geophysical Monographs 55, pp. 165-236, American Geophysical Union, Washington, D.C.
- Lait, L. R. and J. L. Stanford, 1988: Applications of asymptotic space-time Fourier transform methods to scanning satellite measurements. *J. Atmos. Sci.*, **45**, 3784-3809.
- Leovy, C. B., 1964: Simple model of thermally driven mesospheric circulation. *J. Atmos. Sci.*, **21**, 327-341.
- Liou, K.-N., 1980: *An Introduction to Atmospheric Radiation*, Academic Press.
- Luther, F. M. and Y. Fouquart, 1984: The intercomparison of radiation codes in climate models (ICRCCM). WMO Rep, WCP-93, World Meteorological Organization, Geneva.
- Marks, C. J., 1989: Some features of the climatology of the middle atmosphere revealed by Nimbus 5 and G. *J. Atmos. Sci.*, **46**, 2485-2508.
- Matthews, E., 1983: Global vegetation and land use: New high-resolution data bases for climate studies. *J. Clim. Appl. Meteor.*, **22**, 474-487.
- Matthews, E., 1984: Prescription of land-surface boundary conditions in GISS GCM 11: A simple method based on high-resolution vegetation data sets. *NA SATech. Mem.* 86096.
- Meyer, W. D., 1970: A diagnostic numerical study of the semi-annual variation of the zonal wind in the tropical stratosphere and mesosphere. *J. Atmos. Sci.*, **27**, 820-830.
- Murgatroyd, R. J. and R. M. Goody, 1958: Sources and sinks of radiative energy from 30 to 90 km. *Quart. J. Roy. Meteorol. Soc.*, **84**, 225-234.
- Murgatroyd, R. J. and H. Singleton, 1961: Possible meridional circulations in the stratosphere and mesosphere. *Quart. J. Roy. Meteorol. Soc.*, **87**, 125-135.

- Pawson, S. and R. S. Harwood, 1989: Monthly -mean diabatic circulations in the stratosphere, *Quart. J. Roy. Meteorol. Soc.*, **115**, 807-840."
- Reber, C. A., C. E. Trevathan, R. J. McNeal, and M. R. Luther, 1993: The Upper Atmosphere Research Satellite (UARS) mission. *J. Geophys. Res.*, **98**, 10,643-10,647.
- Reed, R. J., 1966: Zonal wind behavior in the equatorial stratosphere and lower mesosphere. *J. Geophys. Res.*, **71**, 4223-4233.
- Roberts, R. E., J. E. A. Selby, and L. M. Biberman, 1976: Infrared continuum absorption by atmospheric water vapor in the 8-12 μm window. *Appl. Opt.*, **15**, 2085-2090.
- Rosenfield, J. E., M. R. Schoeberl, and M. A. Geller, 1987: A computation of the stratospheric diabatic circulation using an accurate radiative transfer model. *J. Atmos. Sci.*, **44**, 859-876.
- Rosenlof, J. H. and J. R. Holton, 1993: Estimates of the stratospheric residual circulation using the downward control principle. *J. Geophys. Res.*, **98**, 10,465-10,479.
- Rossow, W. B. and R. A. Schiffer, 1991: ISCCP cloud data products. *Bull. Amer. Meteorol. Soc.*, **72**, 2-20.
- Rothman, L. S., 1992: The HITRAN molecular database: editions of 1991 and 1992. *J. Quant. Spectrosc. Radiat. Transf.*, **48**, 469-509.
- Russell III, J. M., J. C. Gille, E. M. Remsberg, L. L. Gordley, P. L. Bailey, J. L. Fisher, A. Girard, S. R. Drayson, W. F. J. Evans, and J. E. Harries, 1984: Validation of water vapor results measured by the Limb Infrared Monitor of the Stratosphere experiment on Nimbus 7, *J. Geophys. Res.*, **89**, 5115-5124.
- Salby, M. L., 1982: Sampling theory for synoptic satellite observations. Part I: Space-time spectra, resolution, and aliasing. *J. Atmos. Sci.*, **39**, 2577-2600.

- Santee, M. I., 1993: *The thermal structure, dust loading, and meridional transport in the martian atmosphere during late southern summer*. Ph.D. thesis, California Institute of Technology, Pasadena.
- Santee, M. I. and D. Crisp, 1993: Thermal structure and dust loading of the martian atmosphere during late southern summer: Mariner 9 revisited. *J. Geophys. Res.*, 98, 3261-3279.
- Shine, K., 1987: The middle atmosphere in the absence of dynamical heat fluxes. *Quart. J. Roy. Meteorol. Soc.*, **113**, 603-633.
- Shine, K., 1989: Sources and sinks of zonal momentum in the middle atmosphere diagnosed using the diabatic circulation. *Quart. J. Roy. Meteorol. Soc.*, **115**, 265-292.
- Solomon, S., J. 'T. Kiehl, R. R. Garcia, and W. Grose, 1986: Tracer transport by the diabatic circulation deduced from satellite observations. *J. Atmos. Sci.*, 43, 1603-1617.
- Stephens, G. L., 1978: Radiation profiles in extended water clouds. I: Theory. *J. Atmos. Sci.*, 35, 2111-2122.
- Swinbank, R. and A. O'Neill, 1994: A stratosphere-troposphere data assimilation system. *Mon. Wea. Rev.*, 122, 686-702.
- Takahashi, M., 1984: A 2-dimensional numerical model of the semi-annual zonal wind oscillation, in *Dynamics of the Middle Atmosphere*, eds. J. R. Holton and T. Matsuno, Terra Scientific Publishing Company, 253-269.
- Thekaekara, M. P., R. Kruger, and C. I. Duncan, 1969: Solar irradiance measurements from a research aircraft. *Appl. Opt.*, 8, 1713-1732.
- Warren, S. G., 1982: optical properties of snow. *Rev. Geophys. Space Phys.*, 20, 67-89.

- Waters, J. W., L. Froidevaux, W. G. Read, G. L. Manney, L. S. Elson, D. A. Flower, R. F. Jarnot, and R. S. Harwood, 1993: Stratospheric ClO and ozone from the Microwave Limb Sounder on the Upper Atmosphere Research Satellite. *Nature*, 362, 597-602.
- Wiscombe, W. J., 1980: improved Mie scattering algorithms. *Appl. Opt.*, 19, 1505-1509.
- World Meteorological Organization, 1986: Atmospheric Ozone 1985. *WMO Rep. 16*, Global Ozone Res. and Monit. Proj., Geneva, Switzerland.
- Yang, H., F. Olaguer, and K. K. Tung, 1991: Simulation of the present-day atmospheric ozone, odd nitrogen, chlorine, and other species using a coupled 2-D model in isentropic coordinates. *J. Atmos. Sci.*, 48, 442-471.
- Yulaeva, E., J. R. Holton, and J. M. Wallace, 1994: On the cause of the annual cycle in tropical lower-stratospheric temperatures. *J. Atmos. Sci.*, 51, 169-174.

Table 1

Averaging Periods for Radiative Heating and Residual Circulation Calculations. South-viewing Period is Given First.

Yaw	Label	Averaging Periods
1	S-O 91	September 21-25 & October 2-9, 1991
2	O-N 91	November 6-13 & October 18-25, 1991
3	N-D 91	November 26 - December 3 & December 5-12, 1991
4	Jan 92	January 15-22 & January 6-13, 1992
5	Feb 92	February 6-13 & February 15-22, 1992
6	Mar 92	March 24-31 & March 15-22, 1992
7	A-M 92	April 23-30 & May 2-9, 1992
8	M-J 92	June 15-22 & May 24-31, 1992
9	Jul 92	July 5-12 & July 19-26, 1992
10	Aug 92	August 14-21 & August 5-12, 1992
11	Sep 92	September 13-20 & September 22-29, 1992
12	O-N 92	October 30- November 6 & October 21-28, 1992
13	N-D 92	November 21-28 & November 30- December 6, 1992
14	Jan 93	January 10-17 & January 1-8, 1993
15	Feb 93	February 1-8 & February 10-17, 1993
16	Mar 93	March 20-27 & March 11-18, 1993
17	A-M 93	April 21-25 & April 27- May 4, 1993
18	hi-J 93	May 29 - June 5 & May 20-27, 1993
19	J-J 93	June 30- July 7 & July 9-16, 1993
20	J-A 93	August 9-16 & July 25- August 1, 1993
21	Se) 93	September 9-16 & September 23-30, 1993
22	O-N 93	October 25- November 1 & October 22-23, 1993
23	N-D 93	November 17-24 & November 26 -December 3, 1993
24	D-J 93/94	January 7-14 & December 28 - January 4, 1993/94
25	J-F 94	January 25 & February 5-12, 1994
26		
27		
28		
29		
30		

Table 2

Extratropical Downward Mass Flux at 100 hPa, in Units of 10^8 kg s^{-1} , Calculated Using MLS Data and the Radiation Code, Compared With Results From Rosenlof and Holton (1993) Obtained Using UKMO Data and the Downward Control Method

	NH		SH	
	MLS	UKMO	MLS	UKMO
DJF	85.6	80.6	-2.6	33.4
MAM	19.0	45.7	49.0	30.7
JJA	0	25.7	67.8	30.1
SON	68.6	42.7	7.5	27.6

Note: The extratropics are defined as the region poleward of the lowest latitude at which the vertical velocity is downward (see Fig. 3). In JJA, the residual velocity is upward throughout the northern hemisphere, thus giving zero mass flux. The negative value for the SH in DJF denotes upward flux. In view of our estimate for the annual global mean mass flux ($\approx 4 \times 10^8 \text{ kg s}^{-1}$), this value is not significantly different from zero.

Figure captions

Figure 1. (a) A comparison of thermal cooling rates in the spectral region between 5.26 and 250 μm , computed by means of a line-by-line model (solid line) and the radiative model described in the text (dotted line). The model atmosphere is the ICRCM atmosphere (Luther and Fouquart 1984) with three absorbing gases (CO_2 , O_3 , and H_2O) and the calculations have been performed for clear-sky conditions. (b) A comparison of net heating rates for clear-sky conditions with three gases (solid line) and cloudy conditions with seven gases (dotted line). The model atmosphere is the 30°N average for July 19-26, 1992, as observed by MLS.

Figure 2. Latitude-height sections of (a) temperature tendency $\partial\bar{T}/\partial t$, (b) eddy heating (the second term in equation (5) multiplied by $e^{-\kappa z/H}$) calculated from UKMO meteorological fields, (c) eddy heating calculated from the right-hand side of equation (7) multiplied by $e^{-\kappa z/H}$, and (d) net diabatic heating rate. The time average is for the periods February 1-8, February 1-17, and February 10-17, 1993 for the latitude bands 90°S - 300°S , 30°S - 30°N , and 30°N - 90°N , respectively. Contour levels are $\pm 0.1, 0.3, 0.5, \dots$ K day^{-1} in (a)-(c) and $\pm 0.1, 2, \dots$ K day^{-1} in (d).

Figure 3. The residual vertical velocity at 100 hPa. Solid line: September-October-November (the average for the yaws # 1, 2, 11, 12, 13, 21, 22, and 23), dashed line: December-January-February (yaws # 3, 4, 5, 14, 15, 24, and 25) dotted line: March-April-May (yaws # 6, 7, 16, 17, and 18), dashed-dotted line: June-July-August (yaws # 8, 9, 10, 19, and 20). See Table 1 for a list of yaws and their averaging periods. The SON curve has been smoothed 1-2-1 once in latitude to remove irregularities at southern latitudes. The values poleward of 80° have been obtained by linear extrapolation in latitude,

Figure 4. latitude-height sections of the zonal wind. IT IS EXPECTED THAT SOME PANELS IN THE LAST COLUMN WILL BE FILLED IN THE FINAL VERSION OF THE }'AIE}{.

Figure 5. Same as Figure 4, but for the mass-weighted streamfunction $X^* \equiv 2\pi a \rho_s e^{-z/H} \chi^*$ (in units of 10^9 kg s^{-1}). The contour interval is 0.2 and 0.5 for values lower and greater than 1.0, respectively. The zero-line is thicker and the shading denotes areas of counterclockwise flow. The lowest level has been omitted for clarity.

Figure 6. Same as Figure 4, but for the meridional component of the residual circulation \bar{v}^* .

Figure 7. Same as Figure 4, but for the vertical component of the residual circulation \bar{w}^* .

Figure 8. Same as Figure 4, but for the zonal momentum residual (the 1,11S of equation (1)).

Figure 9. Correlation coefficient between T and \bar{w}^* calculated from the first 25 UARS months. The shading denotes anticorrelation. Within regions where $|r| > 0.6$, the sign of the correlation is certain at the 99% confidence level.

Figure 10. Zonally-averaged time-height sections of (a) temperature, (b) ozone, (c) water vapor, (d) zonal wind, (e) \bar{v}^* , (f) \bar{w}^* , (g) the meridional momentum advection (the second term on the LHS of equation (1)), and (h) the momentum residual (the sum of terms on the LHS of equation (1)), averaged over the latitude band 5°S - 5°N . in panels (b) and (c) the time mean has been taken out.

Figure 11. Same as Figure 4, but for water vapor mixing ratio. Water vapor data are not available for the period June 1- July 16, 1992 and after April 25, 1993.

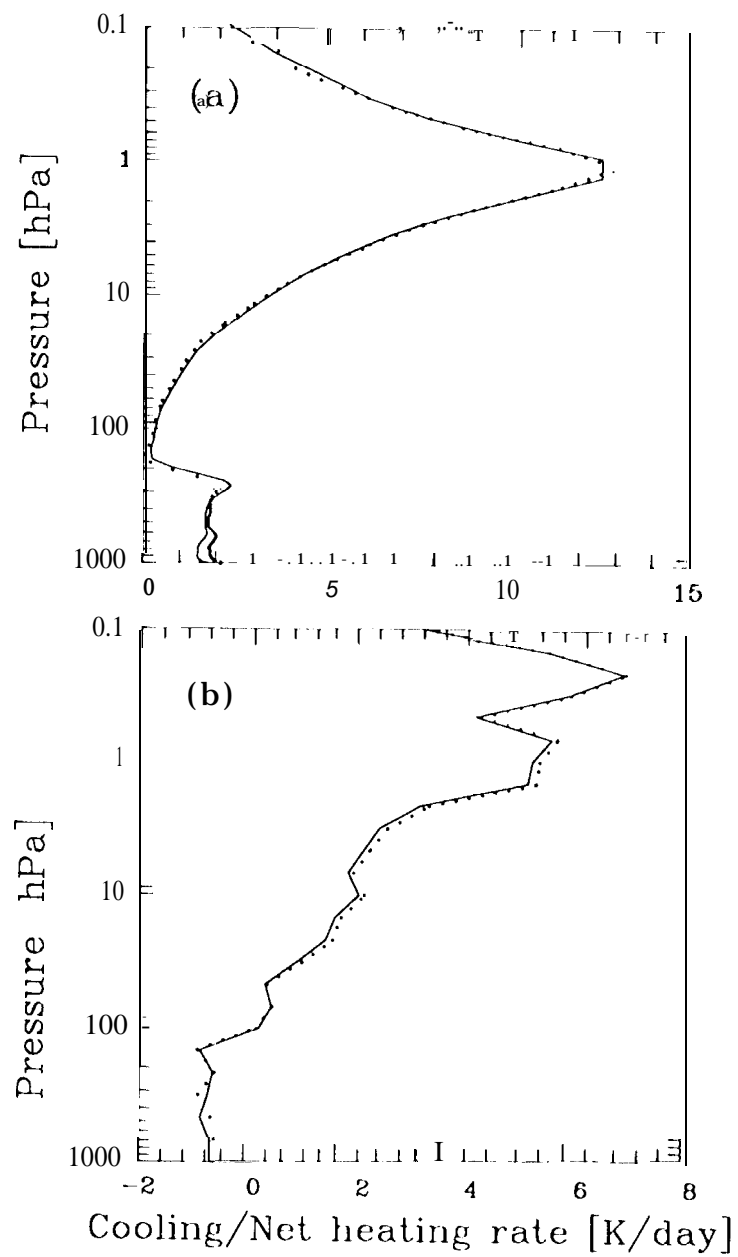


FIGURE 1

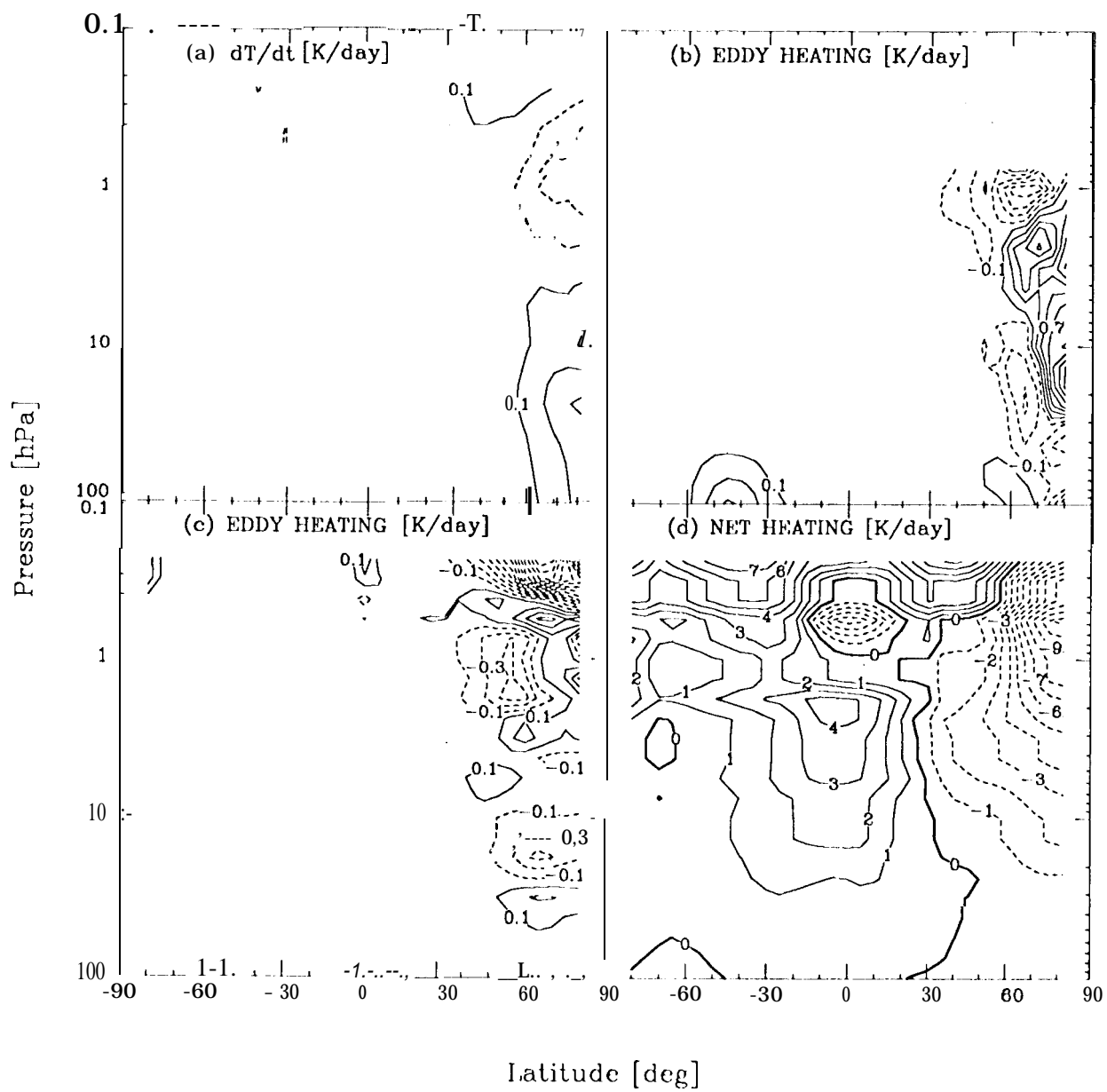


FIGURE 2

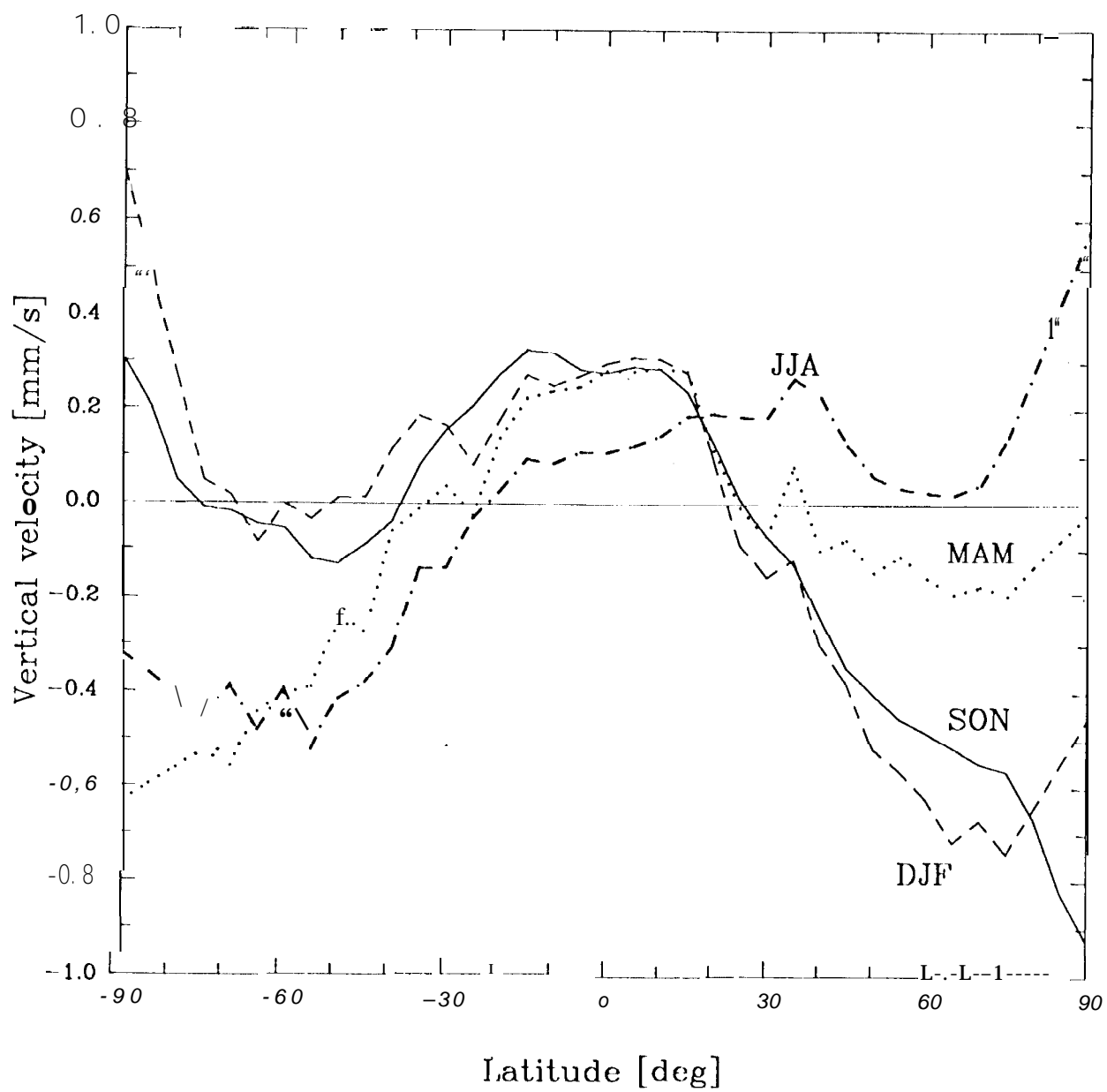


FIGURE 3

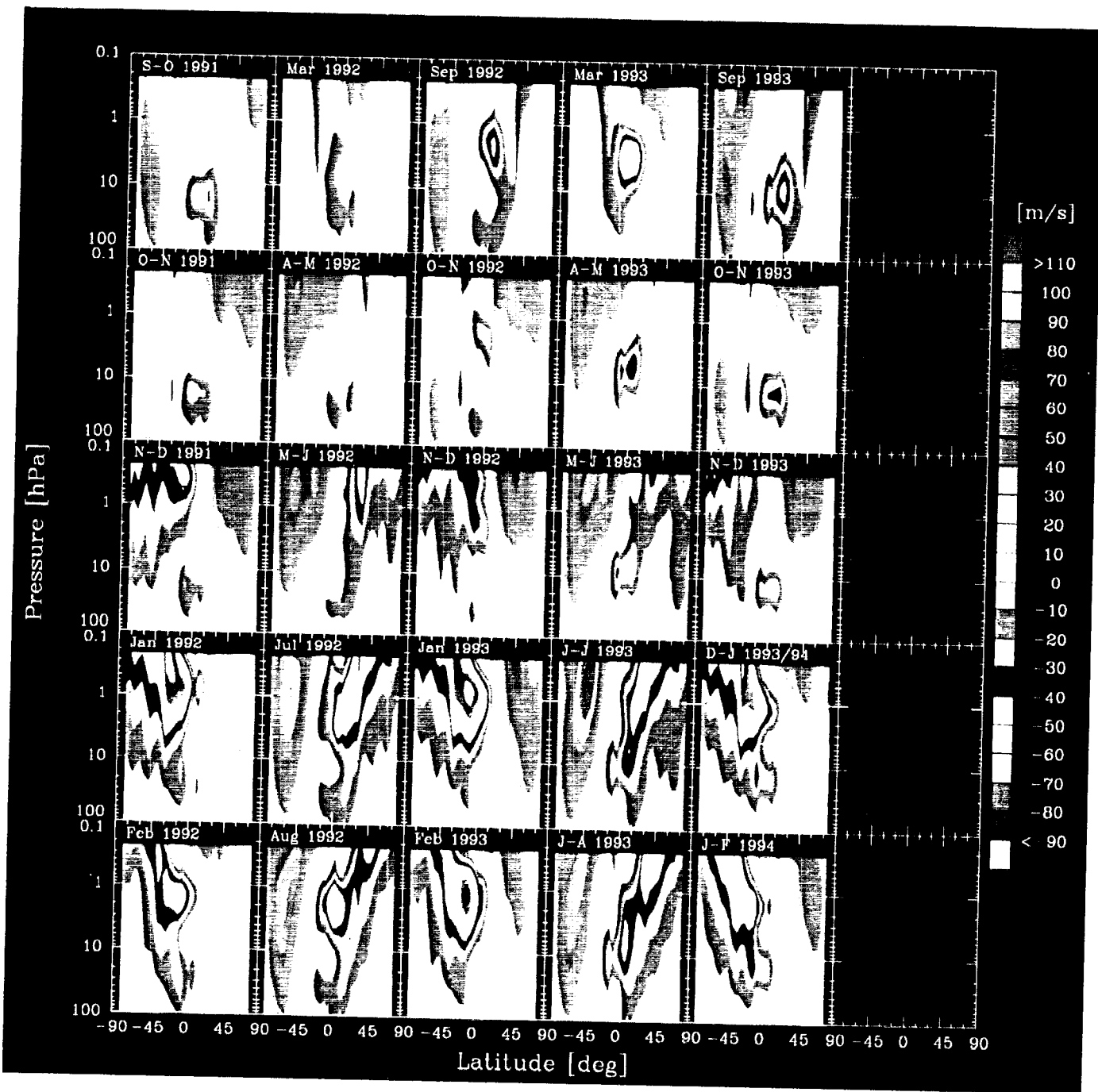


FIGURE 4

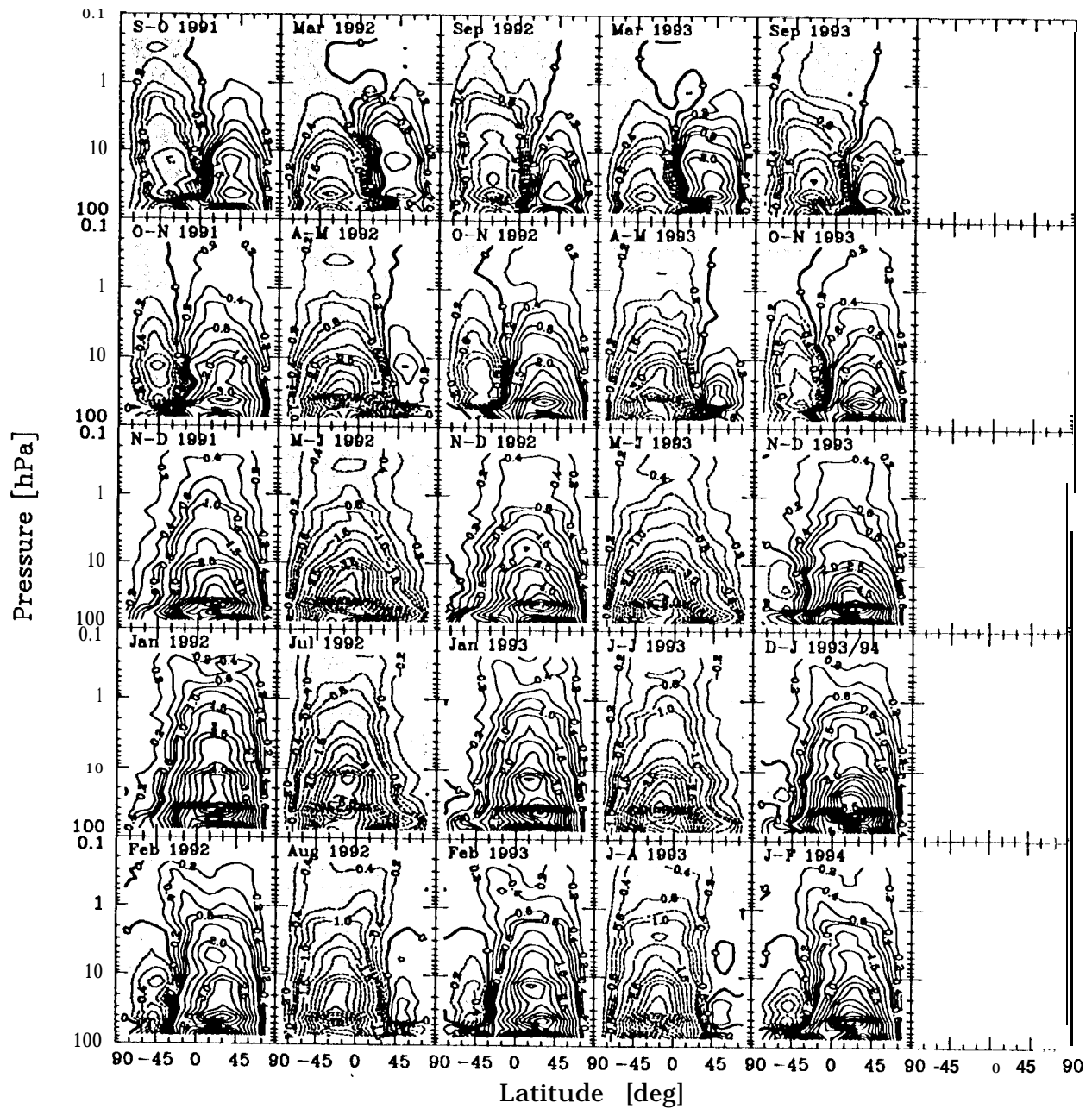


Fig. 5

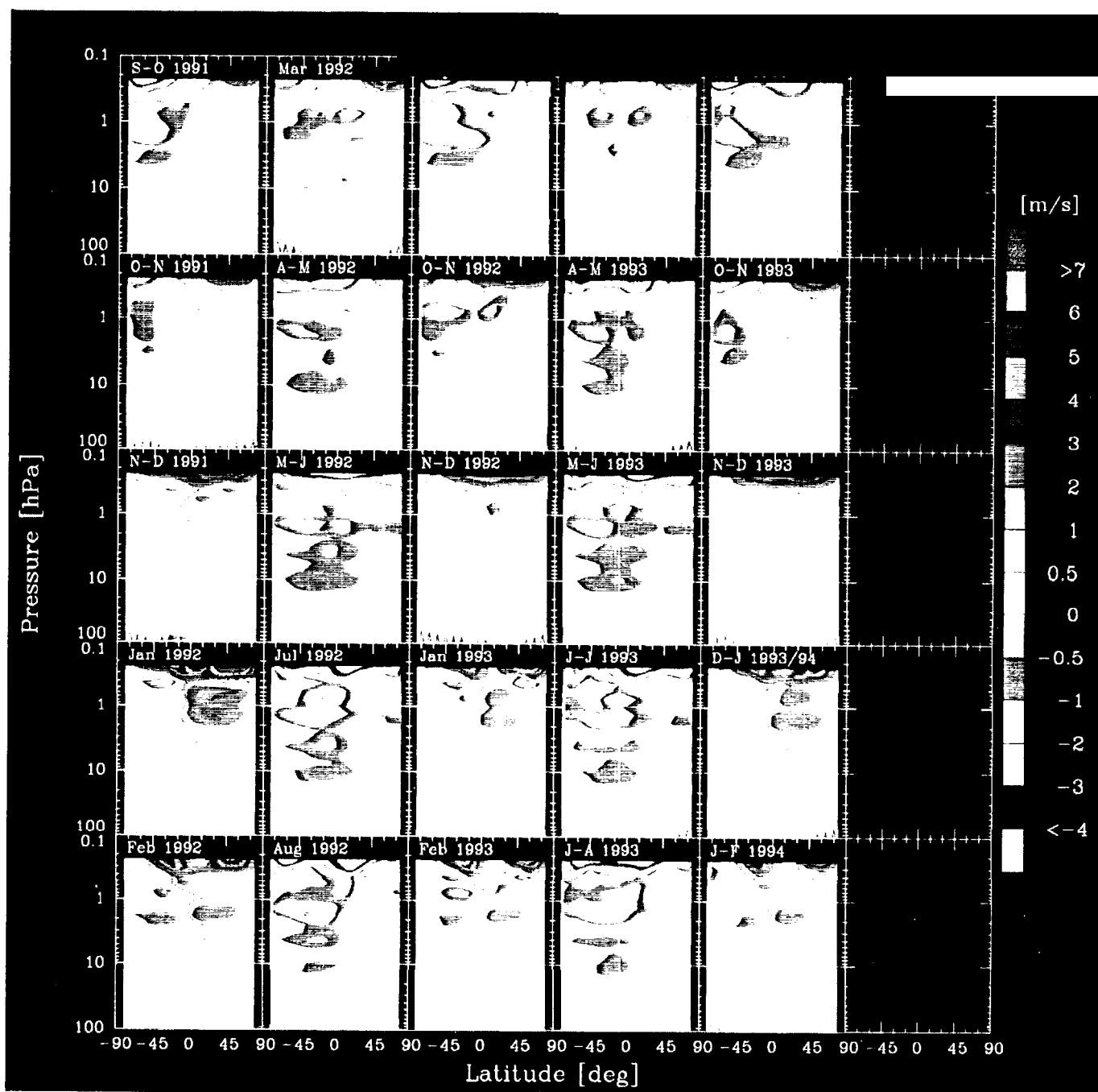


FIGURE 6

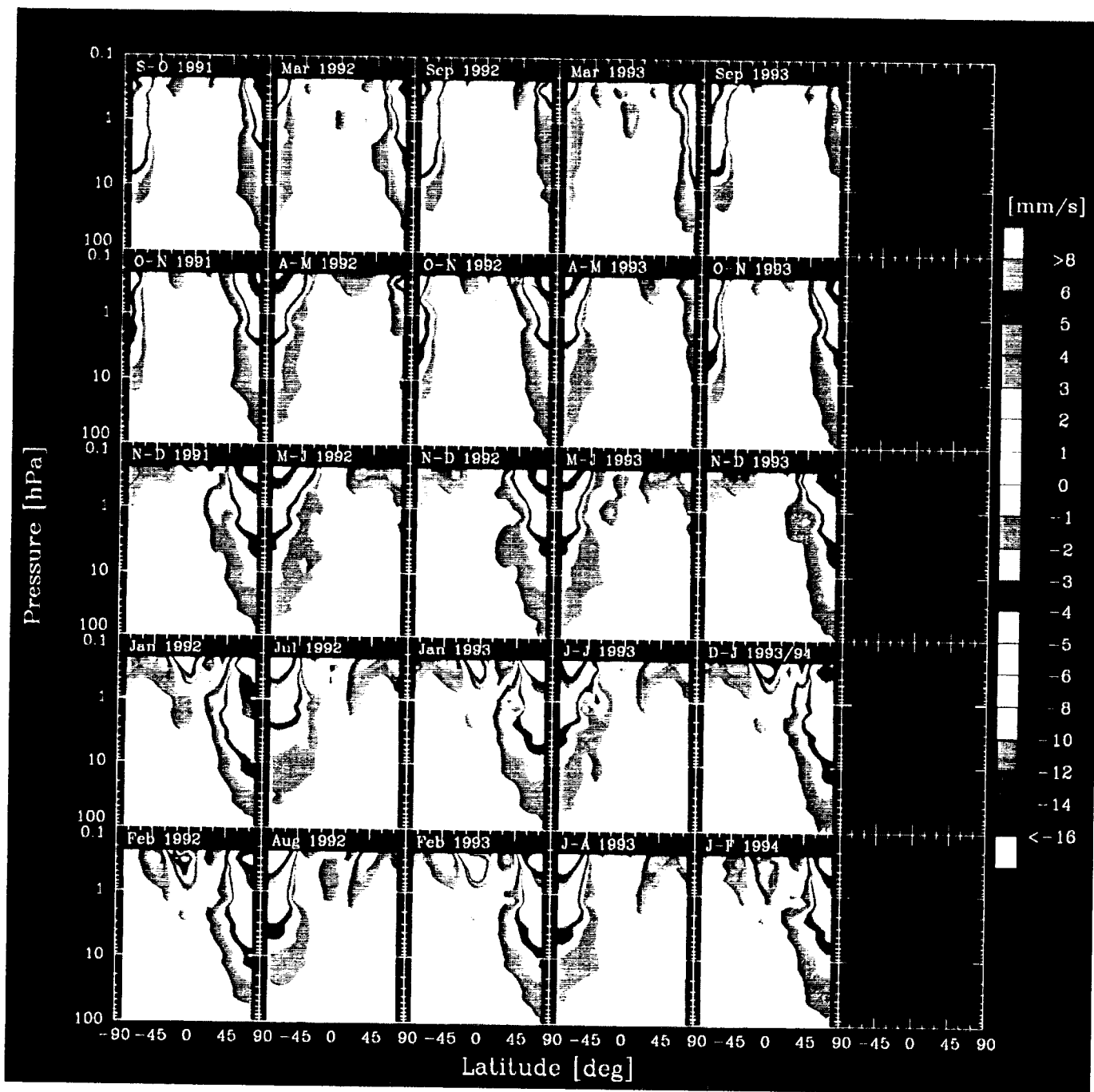


FIGURE 7

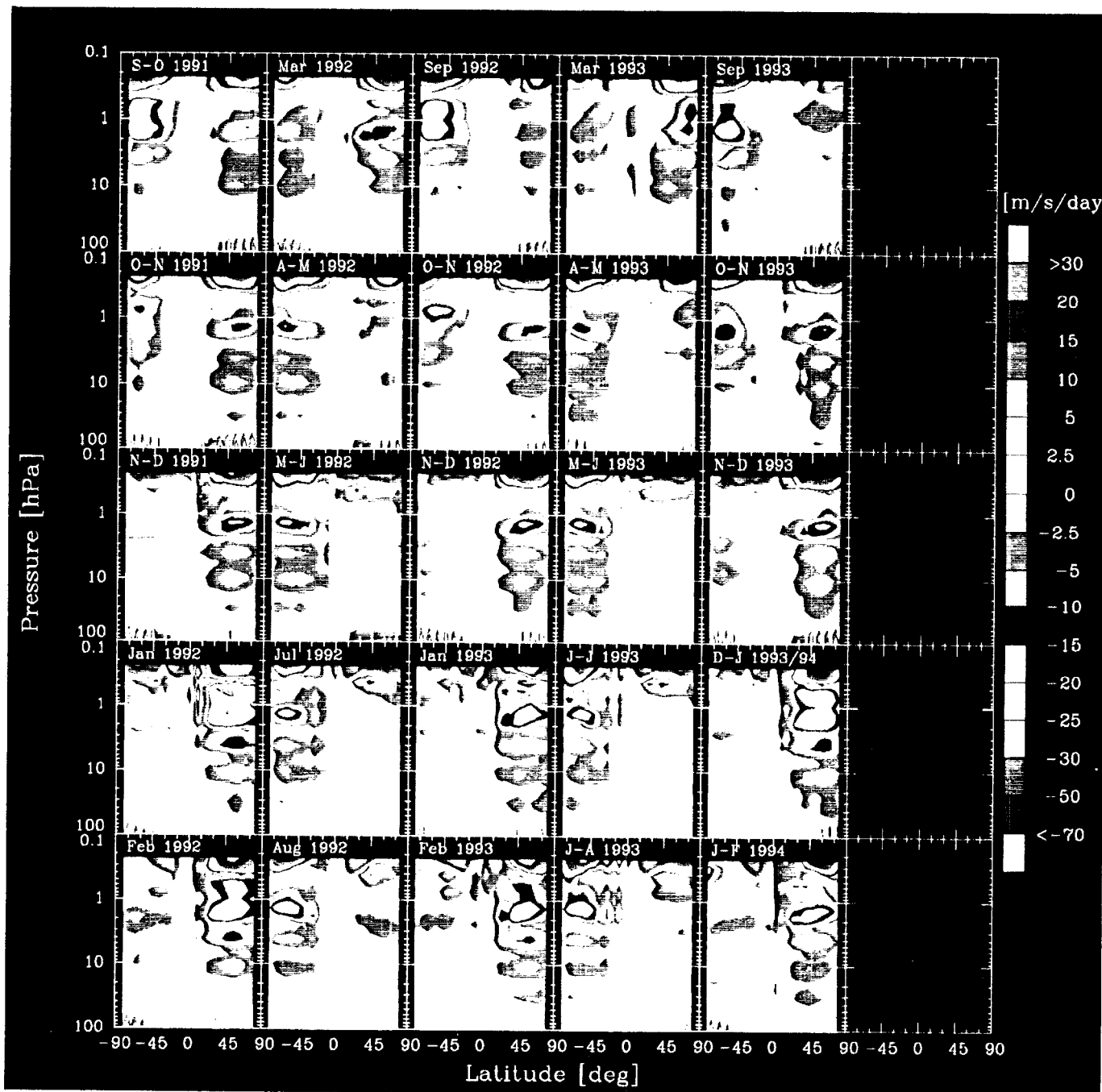


FIGURE 8

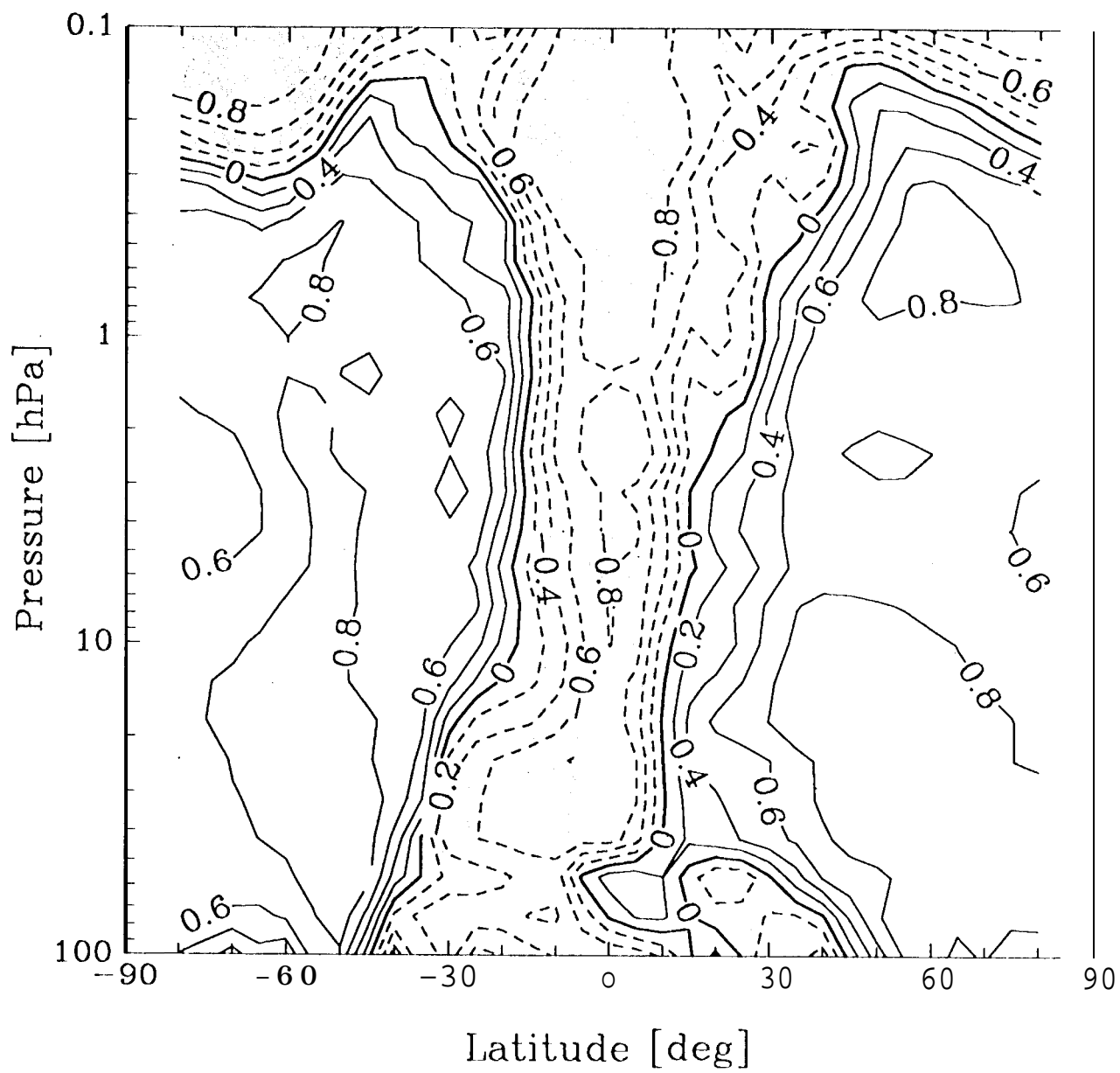


Fig. 9

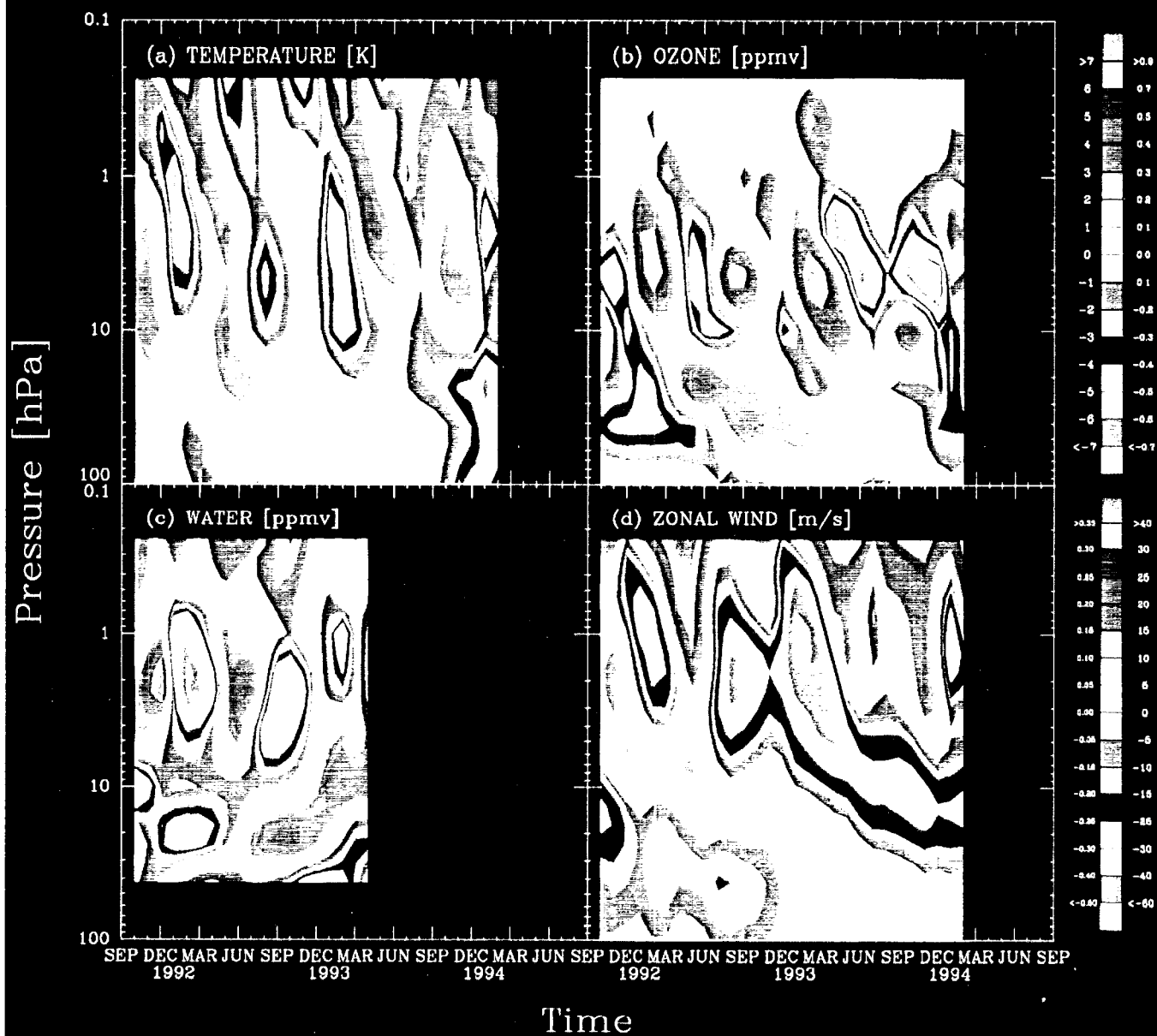


FIGURE 10 a - d

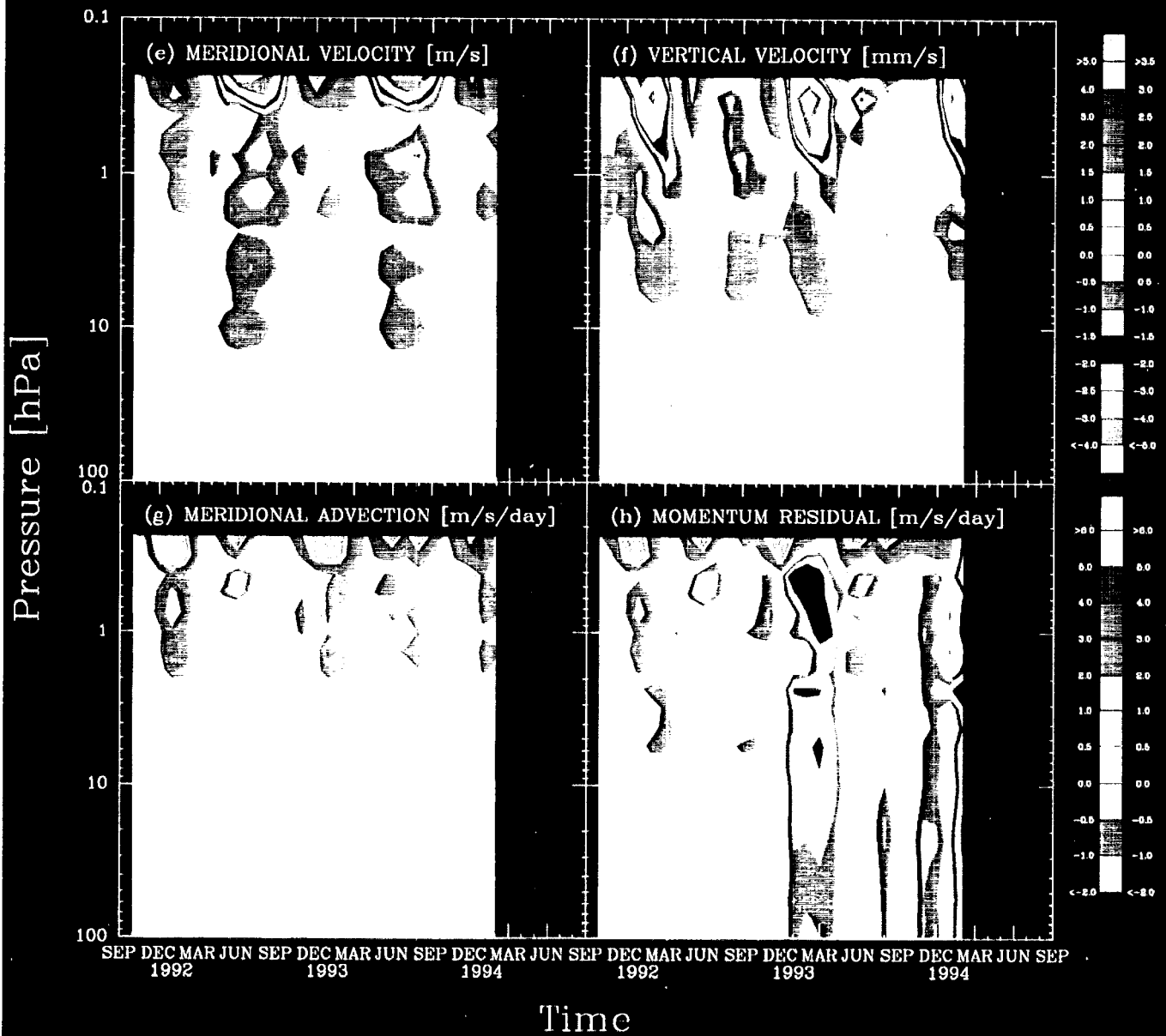


FIGURE 10 c - f

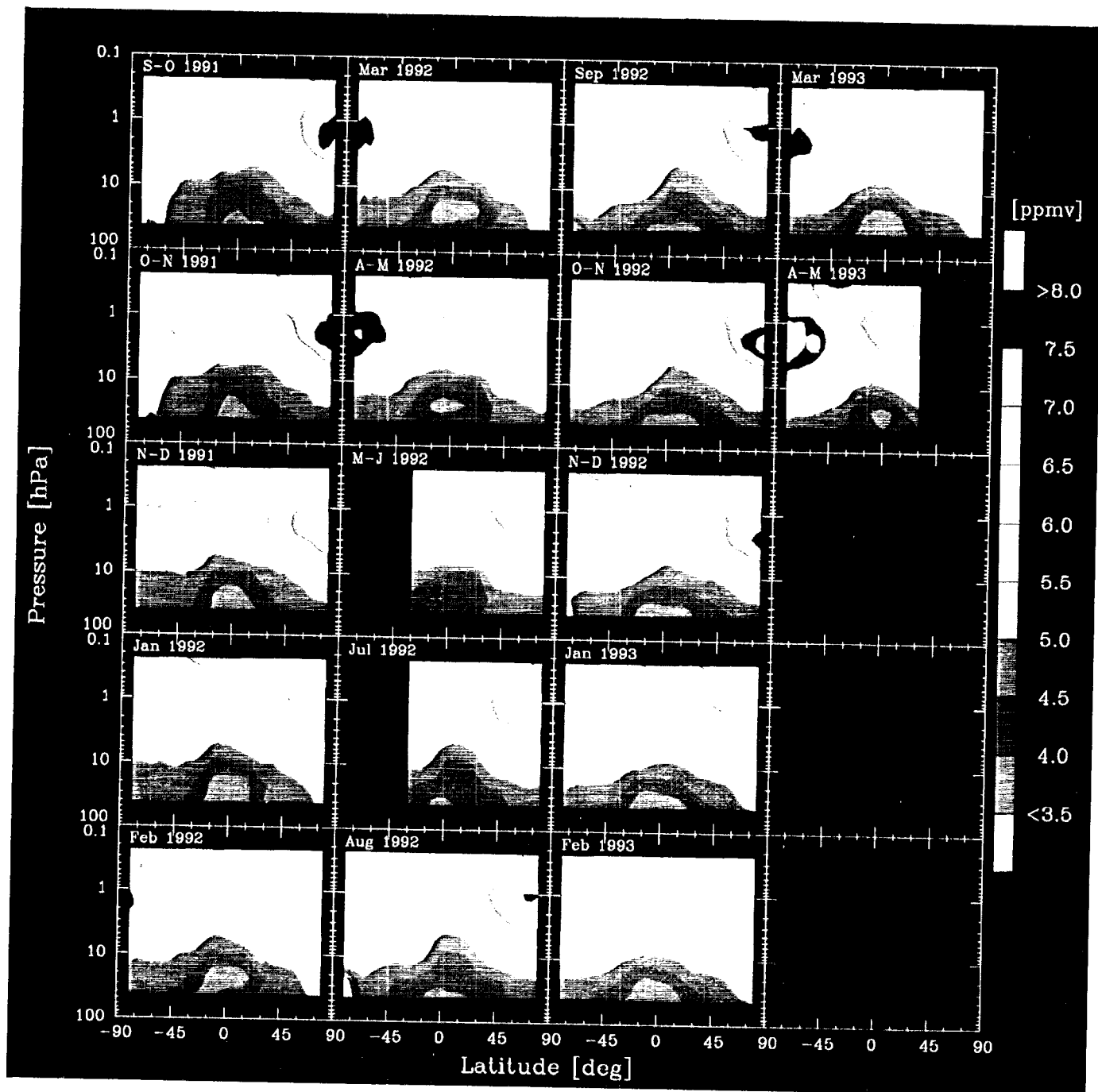


FIGURE 11